


# Evidence for local carbon-cycle perturbations superimposed on the Toarcian carbon isotope excursion

Yunfeng Wang<sup>1</sup>  | Frantz Ossa Ossa<sup>1,2</sup> | Martin Wille<sup>3</sup> | Simon Schurr<sup>4</sup> | Mario-Erich Saussele<sup>1</sup> | Annette Schmid-Röhl<sup>5</sup> | Ronny Schoenberg<sup>1,2</sup>

<sup>1</sup>Department of Geosciences, University of Tuebingen, Tuebingen, Germany

<sup>2</sup>Department of Geology, University of Johannesburg, Johannesburg, South Africa

<sup>3</sup>Institute of Geological Sciences, University of Bern, Bern, Switzerland

<sup>4</sup>Institute of Geology and Paleontology, University of Muenster, Muenster, Germany

<sup>5</sup>Fossil Museum and Werkforum, Holcim (Süddeutschland) GmbH, Dotternhausen, Germany

## Correspondence

Yunfeng Wang, Department of Geosciences, University of Tuebingen, Schnarrenbergstrasse 94-96, 72076 Tuebingen, Germany.  
Emails: yunfeng.wang@uni-tuebingen.de; w727801127@hotmail.com

## Funding information

China Scholarship Council.

## Abstract

A Jurassic negative carbon isotope excursion (CIE), co-evolved with Toarcian Oceanic Anoxic Event (OAE) at ~183 Ma, is suggested to be linked to a global carbon-cycle perturbation and is well documented for Toarcian terrestrial fossil woods and marine sediments around the globe. A theoretically coupled  $\delta^{13}\text{C}_{\text{carb}}-\delta^{13}\text{C}_{\text{org}}$  pattern due to such dubbed global carbon-cycle event from the negative CIE in Dotternhausen Toarcian stratigraphic profile (southwest Germany) is unexpectedly disturbed by two-step  $\delta^{13}\text{C}_{\text{carb}}-\delta^{13}\text{C}_{\text{org}}$  decoupling in which the last step, upper in the stratigraphic order, is of higher magnitude. However, the trigger(s) for these sudden decoupling disturbances are still poorly constrained. Here, connecting new carbon and oxygen isotope data with documentary lipid biomarkers shows that the global carbon cycle during the Toarcian OAE was disturbed by enhanced green sulfur bacteria (GSB) metabolisms and early diagenesis at local scales. The first step  $\delta^{13}\text{C}_{\text{carb}}-\delta^{13}\text{C}_{\text{org}}$  decoupling was induced in the initial stage of the GSB bloom. The second step of much larger  $\delta^{13}\text{C}_{\text{carb}}-\delta^{13}\text{C}_{\text{org}}$  decoupling arising from a GSB prosperity was, however, exaggerated by early diagenesis through the respiration of sulfate-reducing bacteria (SRB). Paleo-geographically distinct localities of the Tethys region show contrasting decoupled  $\delta^{13}\text{C}_{\text{carb}}-\delta^{13}\text{C}_{\text{org}}$  patterns, which implies that the second-order carbon-cycle perturbations have pervasively and independently impacted the global carbon event during the Toarcian OAE.

## KEYWORDS

carbon isotope excursion, green sulfur bacteria, local carbon cycling, Toarcian,  $\delta^{13}\text{C}_{\text{carb}}-\delta^{13}\text{C}_{\text{org}}$  decoupling

## 1 | INTRODUCTION

Sudden and large-magnitude changes in global carbon-cycle perturbations along with carbon isotope excursions (CIEs) seem to be recurrent phenomena during greenhouse periods in Earth's history

(Jenkyns, 2010). One of the considerably negative CIEs in Earth's history occurred during the Early Jurassic, near-contemporaneously with the Toarcian Oceanic Anoxic Event (OAE at ~183 Ma; Jenkyns, 1988). The Toarcian OAE was a time of severe environmental change that was linked to elevated continental weathering rates (Cohen,

[Correction added on 15 September 2020, after first online publication: The order of Figures 4, 5 and 6 has been swapped.]

This is an open access article under the terms of the Creative Commons Attribution License, which permits use, distribution and reproduction in any medium, provided the original work is properly cited.

© 2020 The Authors. *Geobiology* published by John Wiley & Sons Ltd

Coe, Harding, & Schwark, 2004; Percival et al., 2016; Them et al., 2017), marine mass extinctions (Danise, Twitchett, & Little, 2015; Little & Benton, 1995; Wignall et al., 2006), biocalcification crises (Han, Hu, Kemp, & Li, 2018; Trecalli et al., 2012), widespread anoxia (Pearce, Cohen, Coe, & Burton, 2008), and considerable accumulation of organic-rich sediments (Baudin, Herbin, & Vandenbroucke, 1990; Jenkyns, 1988). This event is generally accompanied by a globally synchronous ~3–7‰ negative CIE, expressed in terrestrial fossil wood (e.g., Hesselbo, Jenkyns, Duarte, & Oliveira, 2007), land plant lipids (Ruebsam, Reolid, & Schwark, 2020; Xu et al., 2017), marine carbonates, and organic matters (e.g., Caruthers, Gröcke, & Smith, 2011; Hesselbo et al., 2000; Xu et al., 2018), interrupting a longer term positive excursion (Jenkyns et al., 2002) attributed to the global increase in organic carbon burial (Jenkyns, 2010). It has been constrained that the observed early Toarcian carbon-cycle perturbation to the global-scale exogenic carbon cycle was probably linked to the injection of massive amounts of CO<sub>2</sub> into the atmosphere-ocean system following the emplacement of the Karoo-Ferrar large igneous province (e.g., Svensen et al., 2007) and/or large-scale release of thermogenic/biogenic methane (e.g., Hesselbo et al., 2000; Kemp, Coe, Cohen, & Schwark, 2005). However, so far, the most negative  $\delta^{13}\text{C}_{\text{org}}$  values down to -33‰ during these Toarcian CIEs (e.g., Hesselbo et al., 2000; Kemp, Coe, Cohen, & Schwark, 2005) are not compelling for the typical light carbon isotope compositions of <-35‰ for heterotrophic-derived biomass involving methane as the main carbon source (e.g., Hinrichs, 2002; Raghoebarsing et al., 2006). Nevertheless, considering the confirmed global perturbation of the carbon cycle during the Toarcian OAE and the subsequent equilibration between the dissolved inorganic carbon (DIC) and dissolved organic carbon (DOC) reservoirs, a co-variation between  $\delta^{13}\text{C}_{\text{carb}}$  and  $\delta^{13}\text{C}_{\text{org}}$  would be expected (Knoll, Hayes, Kaufman, Swett, & Lambert, 1986). However, a number of studies have observed unpaired curves between  $\delta^{13}\text{C}_{\text{carb}}$  and  $\delta^{13}\text{C}_{\text{org}}$  records in Toarcian OAE stratigraphic profiles (Fu et al., 2016; Han, Hu, Kemp, & Li, 2018; Hermoso et al., 2012; Röhl, Schmid-Röhl, Oschmann, Frimmel, & Schwark, 2001), indicating that second-order carbon cycles might have played a significant role during the Toarcian OAE. In general, unmatched  $\delta^{13}\text{C}_{\text{carb}}$  and  $\delta^{13}\text{C}_{\text{org}}$  records can be diagnostic for post-depositional diagenetic alteration, hydrocarbon contamination, DOC contribution, terrestrial contamination (Jiang et al., 2012; Maloof et al., 2010), or metabolisms by Chlorobiaceae, such as green sulfur bacteria (GSB), which are anoxygenic phototrophs that are able to oxidize hydrogen sulfide (H<sub>2</sub>S) to sulfate (SO<sub>4</sub><sup>2-</sup>) at low light availability (Riccardi, Kump, Arthur, & D'Hondt, 2007). However, how and to what extent second-order carbon cycling is responsible for the observed Toarcian OAE  $\delta^{13}\text{C}_{\text{carb}}$ - $\delta^{13}\text{C}_{\text{org}}$  decoupling remain poorly constrained. Therefore, little attention has been attributed to carbon-cycle perturbations at a local scale. As such, a more comprehensive understanding of the features of the Toarcian negative CIEs might be, in part, hindered when correlating the Toarcian OAE chemostratigraphy worldwide.

This study re-investigates the nature of the Toarcian CIE for both the DIC and DOC reservoirs at the Toarcian OAE sedimentary section of Dotternhausen, Germany, which is characterized

by well-preserved organic-rich sediments (Röhl, Schmid-Röhl, Oschmann, Frimmel, & Schwark, 2001). Thus, these sediments provide an especially valuable archive for tracking coeval carbon-cycle processes and evolution of the contemporaneous biosphere (Schwark & Frimmel, 2004). To do so, new outcrop and drillcore samples from the Dotternhausen section were sampled at a high-stratigraphic resolution for integrated analyses of bulk  $\delta^{13}\text{C}_{\text{carb}}$ ,  $\delta^{13}\text{C}_{\text{org}}$ ,  $\delta^{18}\text{O}_{\text{carb}}$ , total organic carbon on a carbonate-free base (TOC<sub>cf</sub>), carbonate concentration, and major- and trace-elemental contents. Additionally, we compiled and compared the previously published  $\delta^{13}\text{C}_{\text{carb}}$ - $\delta^{13}\text{C}_{\text{org}}$  records from geographically different Toarcian OAE localities (Bilong Co section in eastern Tethys, Fu et al., 2016; Sancerre section in northwestern Tethys, Hermoso et al., 2012; and Nianduo section in southeastern Tethys, Han, Hu, Kemp, & Li, 2018), in order to investigate whether second-order carbon-cycle processes may have superimposed the Toarcian OAE  $\delta^{13}\text{C}_{\text{carb}}$  and  $\delta^{13}\text{C}_{\text{org}}$  records on a global scale.

## 2 | GEOLOGICAL BACKGROUND

During the Jurassic, most of present-day Europe was located on a broad and shallow continental shelf that deepened toward the south-east Tethys Ocean (Jenkyns, 2010) (Figure 1a). The coeval shallow shelf was marked by several sub-basins within which the water-mass circulation was hydrographically restricted (McArthur et al., 2008; Röhl, Schmid-Röhl, Oschmann, Frimmel, & Schwark, 2001). Moreover, global warming linked to the massive carbon emissions (Cohen, Coe, Harding, & Schwark, 2004; Hesselbo et al., 2000; Kemp, Coe, Cohen, & Schwark, 2005; Ruebsam, Münzberger, & Schwark, 2014; Ruebsam, Mayer, & Schwark, 2019) as well as tectonic activities (e.g., breakup of the Pangaea Supercontinent) may jointly have been responsible for a major marine transgression and deoxygenation during the early Jurassic (Toarcian), at least in the vastly extending shallow marine areas developed by the opening Tethys Ocean. These prominent changes in paleoceanic conditions and paleoclimate were likely responsible for the widespread deposition of organic-rich sediments during that time (e.g., Baudin, Herbin, & Vandenbroucke, 1990).

The Toarcian OAE Dotternhausen sedimentary section (48°13'32.60"N, 8°46'29.76"E), geographically situated in southwestern Germany, represents a mid-paleo-latitude basin, at the southern margins of European epicontinental seaways, which bridged the northwest Tethys Ocean and the Boreal Sea during the Early Jurassic (Ziegler, 1988) (Figure 1b,c). This section exhibits the well-studied, and laterally widespread, Lower Toarcian Posidonia Shales, which are world-famous for their exceptionally well-preserved fossils and their high organic matter content (up to 16 wt.% TOC) (Bour, Mattioli, & Pittet, 2007; Fantasia, Föllmi, Adatte, Spangenberg, & Montero-Serrano, 2018; Montero-Serrano et al., 2015; Ruebsam, Münzberger, & Schwark, 2014; Song, Littke, & Weniger, 2017). The sedimentary rocks are exceptionally well preserved and thus provide an ideal stratigraphic sequence to investigate the Toarcian OAE and compare it with the worldwide negative

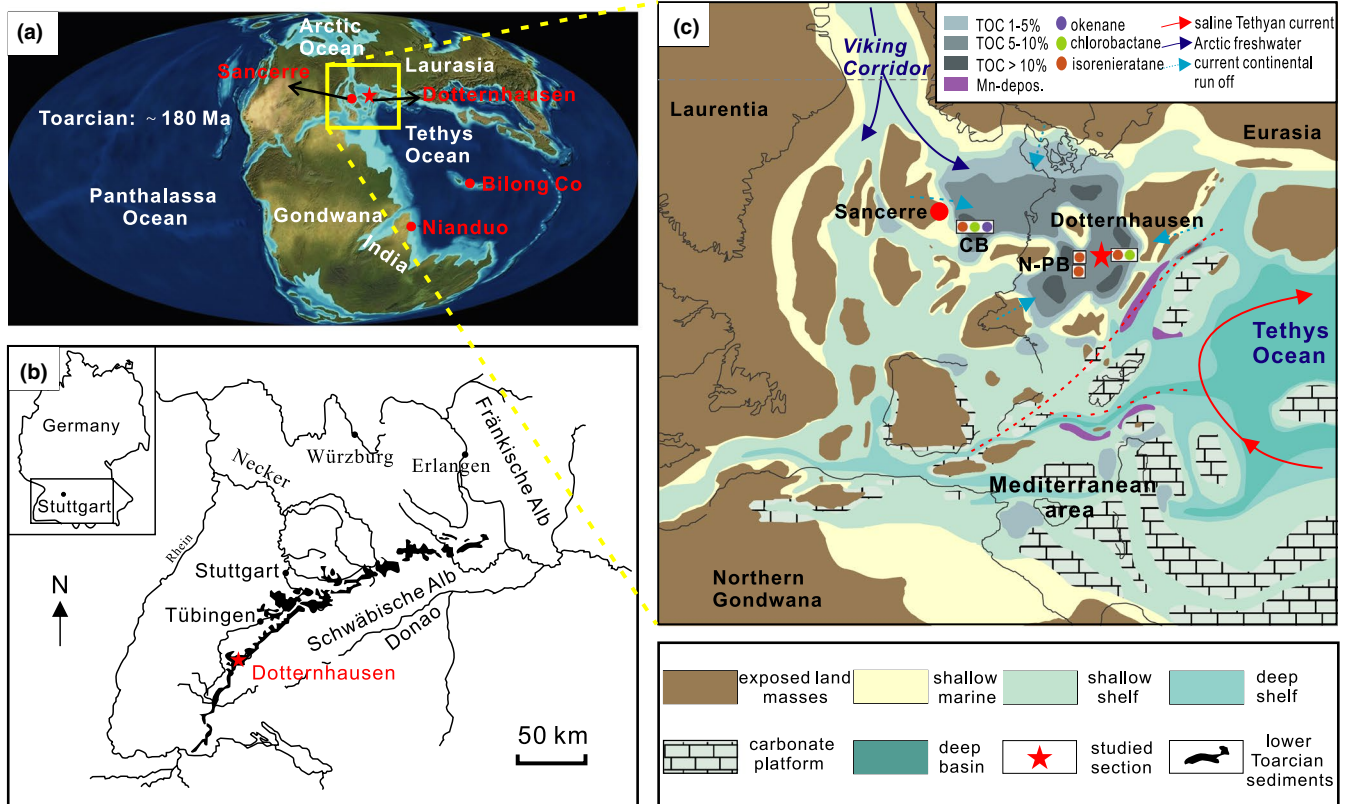


**FIGURE 1** (a) Global paleogeography of the early Toarcian showing northwestern Tethys shelf seas (adapted from Ron Blakey, <http://jan.ucc.nau.edu/~rcb7/>); (b) present location of the studied Dotternhausen quarry (modified after Röhl, Schmid-Röhl, Oschmann, Frimmel, & Schwark, 2001); (c) paleogeography of the northwestern Tethys shelf area, an epicontinental shelf sea that opened toward the Tethys in the southeast (modified after Ruebsam, Münzberger, & Schwark, 2014). During early Toarcian, contrasting paleogeographic settings were probably linked to the influence of different current systems (Bjerrum, Surlyk, Callomon, & Slingerland, 2001; Mattioli, Pittet, Suan, & Mailliot, 2008). Total organic carbon (TOC) and biomarker data in Dotternhausen (red star), Cleveland Basin (CB), and northern Paris Basin (N-PB) are from Schouten, van Kaam-Peters, Rijpstra, Schoell, & Damsté (2000), French et al. (2014) and van Breugel, Baas, Schouten, Mattioli, & Sinninghe Damsté (2006), respectively. The geographically distant localities of Bilong Co, Nianduo and Sancerre (red dots) were compared in this study

CIE records (Röhl, Schmid-Röhl, Oschmann, Frimmel, & Schwark, 2001). The Dotternhausen sedimentary section has been litho- and bio-stratigraphically well characterized, mainly including three ammonite zones (*tenuicostatum*, *falciferum*, and *bifrons*) and some subzones (*elegantulum*, *exaratum*, *elegans*, and *falciferum*; Figure 2), though the transition between the *tenuicostatum* and *falciferum* zones remains not precisely constrained due to a lack of standard fossils and/or to the existing stratigraphic gap in the Pliensbachian-Toarcian boundary interval (Kuhn & Etter, 1994). Furthermore, the whole section has been investigated and subdivided into three contrasting lithofacies units in ascending order: bioturbated mudstones (1,180–980 cm), laminated oil shales (980–550 cm), and bituminous mudstones (550–0 cm), respectively, in terms of the amounts of organic matter and the types of fabric (cf. Röhl, Schmid-Röhl, Oschmann, Frimmel, & Schwark, 2001). This study only shows the sedimentary strata from 1,180 to 560 cm (Figure 2), which include the Toarcian negative CIE. The laminated oil shale unit is largely limited to the uppermost part of *tenuicostatum* zone and the lower and middle parts of the *falciferum* zone (Figure 2), is marked by a complete lack of benthic fauna, and exhibits a distinct micro-lamination.

The laminated oil shale unit is separated by three calcite-rich beds in different thickness, Unterer Stein, Steinplatte, and Oberer Stein from the bottom up (Frimmel, Oschmann, & Schwark, 2004) (Figures 2 and 3a). The thickest one, Unterer Stein (20–30 cm) in the *exaratum* subzone (Figures 2 and 3b), can serve as an efficient stratigraphic marker across Germany, Switzerland, and France within the Lower Toarcian Posidonia Shales in European epicontinental basins/shelves (Kuhn & Etter, 1994; van de Schootbrugge et al., 2005). An increasing body of evidence indicates that the Unterer Stein is an early diagenetic precipitate associated with organic matter remineralization enhanced by bacterial sulfate reduction within the sediment (Röhl and Schmid-Röhl, 2005; Röhl, Schmid-Röhl, Oschmann, Frimmel, & Schwark, 2001). Moreover, the carbonate fraction in the laminated oil shale facies in the Dotternhausen section was primarily derived from the hard parts of calcareous phytoplankton, including coccolithophorids and schizosphaerelle (Röhl, Schmid-Röhl, Oschmann, Frimmel, & Schwark, 2001), which is in contrast to the Unterer Stein bed which comprises only few fecal pellets (figure 5 of Frimmel, Oschmann, & Schwark, 2004). More detailed geological and paleontological descriptions of the Dotternhausen section can

**FIGURE 2** Facies distribution and lamination types of the Dotternhausen section during Toarcian OAE (modified after Röhl, Schmid-Röhl, Oschmann, Frimmel, & Schwark, 2001)

## Dotternhausen Section

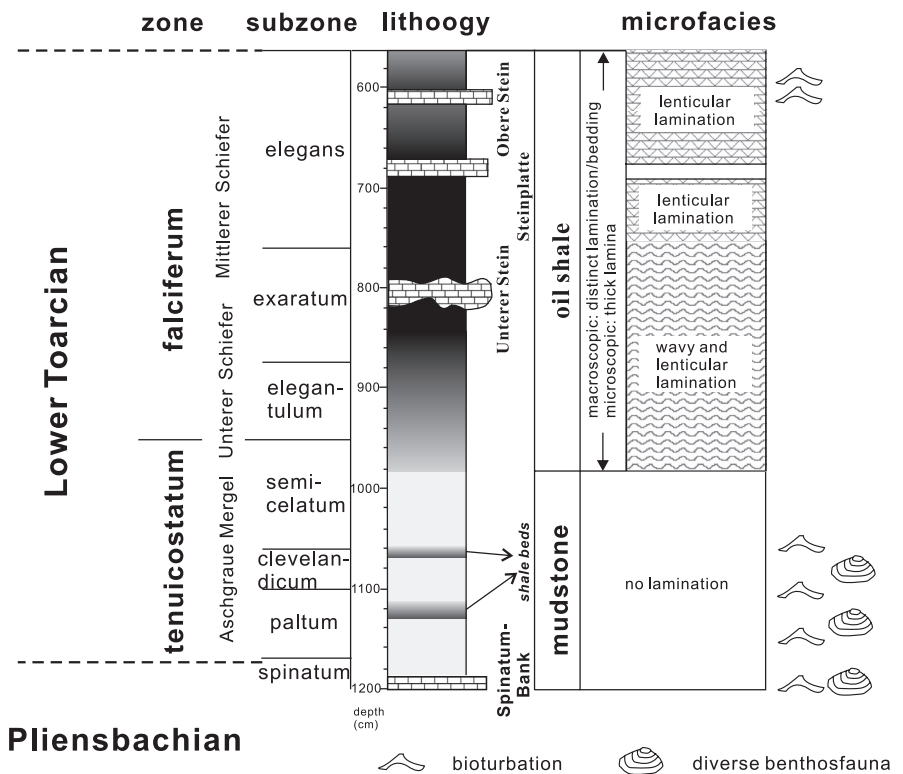
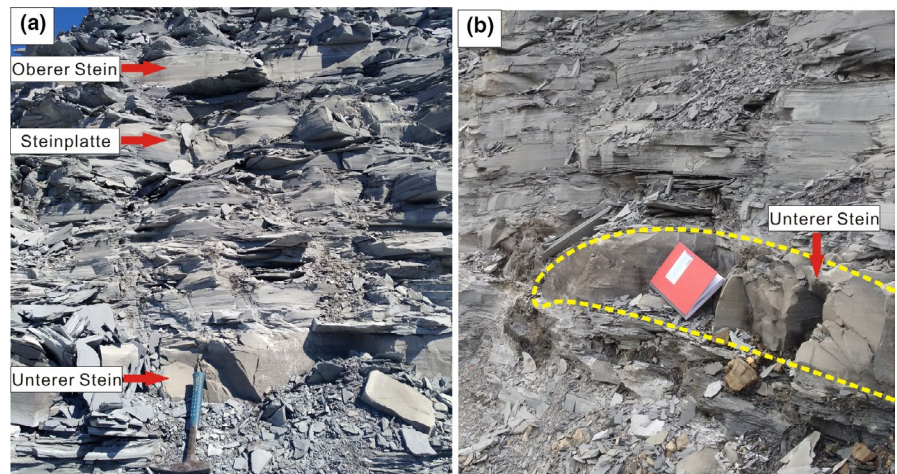


**FIGURE 3** Photographs of the Dotternhausen sedimentary section. (a) Dotternhausen Toarcian CIE black shale facies intercalated by three limestone beds (Unterer Stein, Steinplatte and Oberer Stein). (b) Diagenetic Unterer Stein carbonate bed with the thickness of 20–30 cm



be found in previous publications (cf. Röhl and Schmid-Röhl, 2005; Röhl, Schmid-Röhl, Oschmann, Frimmel, & Schwark, 2001).

### 3 | MATERIALS AND METHODS

Samples of this study include gray mudstones, black shales, and diagenetic limestones taken from the stratigraphic section of the Dotternhausen profile (Figure 2) between depths of 610 m (upper *falciferum* *elegans*, starting with the limestone unit “Oberer Stein”) and 1,010 m (upper *tenuicostatum* *semicelatum*) at a high resolution with an average spacing of 3.5 cm. Notably, outcrop samples were

taken on a freshly quarried surface avoiding the long-term influence from surface weathering and contamination by vegetation. Powders from outcrop and drillcore samples were prepared using a diamond-mounted driller and dried at 60°C for further analyses.

#### 3.1 | Elemental analyses

##### 3.1.1 | Major elements analyses

100 mg sample powders were mixed with 500 mg of Merck Spectromelt® A12 and were heated to 1,050°C for 30 min using

Oxiflux system to prepare homogeneous glass beads. These beads were then dissolved in polypropylene bottles using 100 g of 2%  $\text{HNO}_3$  to a dilution factor of  $\sim 1,000$  and then were diluted with 2%  $\text{HNO}_3$  to obtain a final dilution factor of 1:150,000 for major element concentration measurement. Loss on ignition (LOI) was determined on a separate  $\sim 100$  mg sample aliquot by the weight loss after 60 min of heating in a furnace at  $1,050^\circ\text{C}$ . Analyses were carried out on a Thermo Fisher Scientific iCap-Qc quadrupole inductively coupled plasma mass spectrometer (Q-ICP-MS) using a similar experimental design as described in detail below for the trace element determinations (Section 3.1.2.). Calibration for sample unknowns used the powder reference materials W-2a (United States Geological Survey; USGS) prepared as above and using the major element values reported in Govindaraju & Roelandts (1989). Secondary quality control standards were also prepared from the international reference materials (QS-1, OU-6, SCo-1, and AGV-2), and the precision range of major elements relative to the recommended values from GeoReM. Data are reported as elemental concentrations expressed in weight percent (wt.%), and generally, uncertainties for major elements are better than 1 wt.% ( $1\sigma$ ).

### 3.1.2 | Trace elements analyses

$\sim 200$  mg of dried powder materials was weighted and ashed in a furnace at  $500^\circ\text{C}$  for 15 hr to oxidize organic matter. These ashed sample powders were re-weighed immediately upon cooling to determine the loss of weight during the ashing process.  $\sim 25$  mg of ashed powders was weighed and digested in a 4 ml (4:1) HF- $\text{HNO}_3$  volumetric mixture on hot plates at  $120^\circ\text{C}$  for 2 days. Following digestion, the dissolved sample mixtures were evaporated, and the residues were reacted with 2 ml 6 M HCl at  $120^\circ\text{C}$  for 24 hr to dissolve potential fluorides. Upon drying the samples, they were taken up in 1 ml 14.5 M  $\text{HNO}_3$ , heated to  $120^\circ\text{C}$  for 1 hr and dried again to volatilize excess fluorine and chlorine. This last step was repeated to ensure full conversion of the samples to nitric form. The samples were then taken up in 1 ml 5 M  $\text{HNO}_3$  and gravimetrically diluted to  $\sim 30$  ml 2%  $\text{HNO}_3$  stock solutions with a nominal dilution factor of  $\sim 1,000$ . Powders of rock reference materials used for calibration and quality control were also digested using this procedure. For analyses, all stock solutions were then further diluted with 2%  $\text{HNO}_3$  to a nominal, gravimetric dilution factor of  $\sim 10,000$ . This 2%  $\text{HNO}_3$ , as an internal standard during ICP-MS analysis, contains a mixed spike of  $^6\text{Li}$  ( $\sim 3$  ng/g), In ( $\sim 1$  ng/g), Re ( $\sim 1$  ng/g), and Bi ( $\sim 1$  ng/g). All samples were measured using a Thermo Fisher Scientific iCap-Qc ICP-MS coupled to an ESI SC-2 DX autosampler with an ESI Fast uptake system equipped with a 4 ml sample loop. All sample liquids were introduced from the loop using the iCap-Q peristaltic pump (at 30–35 rpm) and aspirated with a PFA nebulizer into a Peltier-cooled cyclonic spray chamber. The nebulizer and cool gas flow rates were typically  $\sim 1$  and 14 L/min, respectively, and the interface was configured with Ni sampler cone, with a Cu core and Ni skimmer cone with a high-matrix insert.

The analytical procedure was analogous to that described in previous studies (Albut et al., 2018; Babechuk, Widdowson, Murphy, & Kamber, 2015; Kamber, Webb, & Gallagher, 2014). Oxide/hydroxide interference rates of Ba on Eu, Nd on the MREE to HREE (Gd, Tb, Dy, Er), Zr, on Ag, and the isobaric overlap of  $^{160}\text{Dy}$  on  $^{160}\text{Gd}$  were quantified ahead of each experiment. Remaining interference “rates” were determined according to a previous quantification scaled to the daily Nd oxide on Gd production rate (Aries et al., 2007; Ulrich, Kamber, Woodhead, & Spencer, 2010). A daily measurement of the  $^6\text{Li}/^7\text{Li}$  ratio in unspiked USGS standard AGV-2 was also applied to determine a correction factor for the contribution of natural  $^6\text{Li}$  in sample unknowns. Experimental sequences contained measurements of the internal standard-bearing carrier acid, procedural blanks, rock calibration (W-2a), and quality control standard (OU-6, QS-1, BCR-2, BHVO-2, BIR-1, and IF-G), sample unknowns, and a final batch of standards. Repeated measurement of a monitor solution (mixture of dissolved rock standards) was made every 5–7 samples for external drift correction remaining after internal standard spike correction. Following the introduction of each sample liquid into the ICP-MS, the sample uptake probe and tubing were rinsed with 5%  $\text{HNO}_3$ . Additional washing with acid blank bracketed monitor samples or was placed between samples known or expected to have contrasting matrices or analyte abundance. In the course of experiments, analyte isotopes were measured in the iCap-Q STD mode, typically with five repeats of 25–30 sweeps at 3 channels (0.1 amu spacing) and analyte dwell times ranging from 10–30 ms. Mean analyte intensities were corrected offline for blank, isobaric interferences, and signal drift. Corrected intensities were calibrated using the average response of repeated measurements (5–8) of the USGS reference material W-2a at different dilution factors ( $\sim 10,000$ ,  $\sim 20,000$ , and  $\sim 40,000$ ), which was prepared from at least three separate powder digestions. The calibration lines that show tighter ranges were constructed using the laboratory's preferred analyte concentrations for the W-2a standard. The overall intermediate method precision and accuracy are monitored using the repeated measurements of reference materials (OU-6, QS-1, BCR-2, BHVO-2, BIR-1, and IF-G), representing a range in analyte concentrations and sample matrices. The method precision, estimated from the 1 r.s.d of the mean, is better than 3% for most elements.

### 3.2 | $\text{TOC}_{\text{cf}}$ and carbonate content analyses

To avoid biases related to carbonate ( $\text{CaCO}_3$ ) dilution, this study reports carbon-free total organic carbon contents ( $\text{TOC}_{\text{cf}}$ ). Powdered mudstone and shale samples had thus to be decarbonized in 15-ml centrifuge tubes by drop-wise addition of 16% HCl at room temperature to remove all inorganic carbon. The residual samples were then centrifuged for 10 min at 246 g, decanted and again mixed with approximately 10 ml Milli-Q  $\text{H}_2\text{O}$ . This procedure was repeated 7–10 times until the samples were neutralized. Upon complete drying of the samples, between 5 and 70 mg of decalcified samples were weighed into tin-capsules.  $\text{TOC}_{\text{cf}}$  concentrations

were performed with a VARIO EL Elemental Analyzer at Center for Applied Geosciences, University of Tuebingen, Germany. Acetanilide standard ( $C_8H_9NO$ , 71.9% Carbon, 10.36% Nitrogen) was analyzed at the beginning, middle, and end of each sample set. All the measured  $TOC_{cf}$  contents were reported as a weight percent (wt.%) of the total fraction, and the external reproducibility is better than 1 wt.% ( $1\sigma$ ). Decalcifying procedures refer to organic carbon isotopic analysis (see below).

For the carbonate content measurement, the treatment procedures for the studied samples are described below for  $\delta^{13}C_{carb}$  (Section 3.3). An almost perfect linear correlation ( $R^2 = .9917$ ) between samples weight (for samples between 10 and 150 mg  $CaCO_3$ ) and the 2nd peak area on the Finnigan MAT 252 gas source mass spectrometer (for further details see Spötl & Vennemann, 2003) allows for the calculation of the carbonate content in each specific sample. These calculated carbonate contents were then divided by total sample weights and multiplied with 100 to obtain the carbonate contents of the bulk samples in %.

### 3.3 | Bulk isotopic analyses

Carbonate fractions of the selected samples were measured for their  $\delta^{13}C_{carb}$  and  $\delta^{18}O$  compositions using a Finnigan MAT 252 gas source mass spectrometer combined with a Thermo-Finnigan Gasbench II/CTC Combi-Pal autosampler at the Isotope Geochemistry Laboratory, University of Tuebingen. Both devices are connected using the continuous flow technique with a He stream as carrier gas. ~50 mg gray mudstone and shale powders, and ~5 mg diagenetic limestone powders were loaded into 10-ml glass vials, sealed with a rubber septum. The vials were then placed in an aluminum tray and heated to 90°C. 20 drops of 99% phosphoric acid were added into the vials, after purging them with pure He gas. After 90 min' reaction time, the released  $CO_2$  was transferred to the mass spectrometer using a He carrier gas via a GC gas column to separate other components. The collected  $CO_2$  was analyzed relative to international reference materials (NBS18,  $\delta^{13}C_{carb} = -5\text{‰}$ ,  $\delta^{18}O = -22.96\text{‰}$  and NBS19,  $\delta^{13}C_{carb} = 1.95\text{‰}$ ,  $\delta^{18}O = -2.20\text{‰}$ ) and an internal laboratory tank gas standard, which was calibrated against the in-house Laaser marble reference material. All measured values are given in per mille (‰) notation relative to the Vienna PeeDee belemnite standard reference material (VPDB) for  $\delta^{13}C$  and VPDB for  $\delta^{18}O$ . The repeatability and intermediate precision of the analyses were monitored by replicate measurements of the laboratory standard Laaser marble and the NBS18 and NBS19. All analyzed results have a reproducibility of  $\pm 0.1\text{‰}$  ( $1\sigma$ ) for both  $\delta^{13}C_{carb}$  and  $\delta^{18}O$ .

Analyses of  $\delta^{13}C_{org}$  were conducted on an Elemental Analyzer NC2500 connected to a Thermo Quest Delta Plus XL mass spectrometer in continuous flow online-mode at the Isotope Geochemistry Laboratory, University of Tuebingen. ~100 mg of sample powders was decalcified in 15-ml centrifuge tubes by drop-wise addition of 16% HCl to remove all inorganic carbon (TIC). Decalcified samples containing

0.05 mg carbon were weighed in tin capsules and combusted at 1,050°C in an oxidation tube and at 650°C in a reduction tube, before they were cooled in a watertrap and transferred through a GC gas column into the mass spectrometer. Sample organic carbon was measured relative to an internal acetanilide standard which is calibrated against an in-house (e.g., Laaser marble) and international reference material (USGS24,  $\delta^{13}C_{org} = -16.00\text{‰}$ ).  $\delta^{13}C_{org}$  results have an external reproducibility of  $\pm 0.1\text{‰}$  ( $1\sigma$ ) for shale and  $\pm 0.2\text{‰}$  ( $1\sigma$ ) for limestones.

## 4 | RESULTS

### 4.1 | Element geochemistry

The concentrations of major element oxides and trace element data of the measured samples from Dotternhausen are reported in Table 1. Aluminum oxide ( $Al_2O_3$ ) in these Dotternhausen samples has a relatively low abundance (mean = 9.43 wt.%) (Table 1) compared to the upper continental crust (UCC: 15.4 wt.%) (McLennan, 2001). Except the Unterer Stein carbonate bed where manganese (Mn) concentration approaches 0.2 wt.%, the Dotternhausen Toarcian OAE profile remains relatively lower than that of the UCC (Table 1; Figure S1). The abundances of immobile trace elements thorium (Th), zirconium (Zr), and scandium (Sc) have a range of 5.1–11.4  $\mu\text{g/g}$ , 64.7–184.3  $\mu\text{g/g}$ , and 9.4–21.3  $\mu\text{g/g}$ , respectively (Table 1). Relative to the UCC (Th: 10.7  $\mu\text{g/g}$ , Zr: 190  $\mu\text{g/g}$ , and Sc: 13.6  $\mu\text{g/g}$ ) (McLennan, 2001), the studied samples display low contents of Th (mean = 9.3  $\mu\text{g/g}$ ) and Zr (mean = 123.2  $\mu\text{g/g}$ ; Table 1), whereas the mean concentration of Sc (16.4  $\mu\text{g/g}$ ) approaches that of the UCC (McLennan, 2001). The Th/Sc and Zr/Sc ratios ranging from 0.38 to 0.67 and 4.65 to 9.33, respectively, show no large variations (Figure 4). The total rare earth element concentrations ( $\Sigma\text{REEs}$ ) vary from 141.9 to 273.8  $\mu\text{g/g}$ , with an average of 210.1  $\mu\text{g/g}$  (Table 1) which is higher than that of the UCC (168.1  $\mu\text{g/g}$ ) (McLennan, 2001). Yttrium (Y) and holmium (Ho) geochemical twins due to their similar radius and charge generally have chondritic Y/Ho values of ~28 in clastic sedimentary rocks (see Albut et al., 2018 and references therein). The studied samples have mildly fluctuating Y/Ho ratios ranging from 25.1 to 31.1 with a mean of 26.8 (Figure 4) which is slightly lower than the chondritic value of ~28. Redox-sensitive elements (molybdenum (Mo), uranium (U), and vanadium (V)) range from 0.93 to 43.8  $\mu\text{g/g}$ , 2.7 to 19.1  $\mu\text{g/g}$  and 99.2 to 463.4  $\mu\text{g/g}$ , respectively (Table 1; Figure S1). In general, the enrichment or depletion pattern of trace element concentrations with respect to the reference material is critical to reconstruct paleoenvironmental conditions (Tribouillard, Algeo, Lyons, & Riboulleau, 2006). In order to trace the authigenic fraction of elements, normalization to an index of the detrital component, normally Al, is necessary (Francois, 1988). The Al concentration of the UCC used for this study is from McLennan (2001). The enrichments of Mo, U, and V are shown in Figure 5. The gray bioturbated mudstones almost do not display enrichments in Mo, U, and V, whereas these elements are obviously enriched in the laminated oil shale facies corresponding to the Toarcian OAE and associated CIE (Figure 5).

TABLE 1 ICP-MS data for Dotternhausen samples

Depth (cm)	613	621	635	638	642	648	656	670	673	680	684	687	698	705
Major [wt. %]														
SiO <sub>2</sub>	33.31	28.52	29.20	25.12	23.44	25.12	25.97	24.60	24.60	21.37	23.60	23.60	26.49	26.35
TiO <sub>2</sub>	0.54	0.49	0.47	0.41	0.40	0.41	0.43	0.41	0.41	0.31	0.39	0.39	0.41	0.42
Al <sub>2</sub> O <sub>3</sub>	10.10	8.75	8.82	7.38	7.05	7.38	7.79	7.48	7.48	6.40	7.07	7.07	7.63	7.99
Fe <sub>2</sub> O <sub>3</sub>	3.82	6.91	3.82	3.63	4.23	3.63	4.63	3.97	3.97	3.29	3.75	3.75	4.44	3.95
MnO	0.06	0.04	0.05	0.05	0.04	0.05	0.04	0.05	0.05	0.05	0.05	0.05	0.05	0.05
MgO	2.05	1.45	2.07	1.17	1.19	1.17	1.12	1.63	1.63	1.45	1.22	1.22	1.30	1.53
CaO	20.89	18.21	21.89	24.12	24.38	24.12	22.91	21.92	21.92	28.48	25.02	25.02	23.73	23.44
Na <sub>2</sub> O	0.30	0.27	0.26	0.23	0.21	0.23	0.23	0.23	0.23	0.17	0.20	0.20	0.22	0.23
K <sub>2</sub> O	1.92	1.55	1.62	1.24	1.22	1.24	1.22	1.29	1.29	1.07	1.11	1.11	1.18	1.40
P <sub>2</sub> O <sub>5</sub>	0.08	0.06	0.06	0.14	0.07	0.14	0.03	0.04	0.04	0.15	0.07	0.07	0.09	0.05
LOI	26.22	33.37	29.42	34.39	35.39	34.39	35.21	35.27	35.27	33.44	34.70	34.70	34.44	33.70
Total sum	99.3	99.6	97.7	97.9	97.6	97.9	99.6	96.9	96.9	96.2	97.2	97.2	100.0	99.1
Trace [µg/g]														
Li	33.0	37.9	31.7	31.7	38.8	31.7	30.7	34.2	40.7	27.3	34.7	32.5	30.4	37.0
Be	2.4	2.6	2.2	2.0	2.5	2.0	1.9	2.3	2.7	1.9	2.3	2.1	2.0	2.5
Sc	15.0	15.3	14.8	14.3	15.0	13.4	12.2	14.2	15.8	12.6	14.9	14.9	14.3	15.7
V	164.1	213.3	145.9	194.3	250.2	224.3	226.2	185.9	242.2	166.3	218.0	215.9	212.3	232.6
Cr	80.8	93.7	77.7	80.6	90.5	72.0	71.8	75.2	96.2	58.4	80.9	73.1	70.6	95.7
Co	14.5	30.9	20.4	39.6	39.6	21.8	32.6	28.3	34.7	18.8	28.1	26.4	30.5	27.9
Ni	50.5	85.1	48.1	94.9	88.2	73.2	84.1	83.2	96.5	67.4	111.6	102.6	86.7	99.8
Cu	48.0	89.3	66.7	96.2	99.4	101.2	96.2	80.8	99.3	54.4	91.6	81.6	83.4	88.3
Zn	39.2	163.7	61.2	184.9	165.9	143.9	120.9	84.0	148.7	510.3	144.8	147.0	142.8	126.1
Ga	14.4	17.8	13.6	15.1	17.7	15.4	14.7	15.9	20.0	12.5	16.2	15.3	15.0	16.7
As	19.1	36.4	25.2	28.5	60.3	17.9	19.2	21.7	25.6	15.2	21.4	18.8	19.9	18.7
Rb	95.3	103.3	86.6	83.8	102.1	79.1	79.6	88.4	109.5	70.2	90.2	82.7	78.4	95.8
Sr	3,623.8	2,670.8	2,002.9	2,407.0	1,481.4	2,065.0	2,201.2	2,242.0	2,164.2	4,350.7	2,361.2	1,667.4	1,072.5	809.1
Y	21.9	25.0	24.0	25.4	24.3	36.2	21.6	24.8	27.7	25.1	28.5	33.5	37.8	30.7
Zr	101.2	115.5	87.1	99.5	125.8	105.7	102.1	103.3	135.7	75.8	109.1	102.9	103.2	113.9
Nb	12.4	14.1	10.8	11.9	14.8	12.6	11.5	12.0	16.2	9.2	13.2	12.1	11.9	14.0
Mo	5.5	13.6	6.0	16.0	23.4	15.9	20.1	14.4	21.6	11.3	19.4	18.7	16.8	21.4
Cd	0.1	0.6	0.2	0.7	0.6	0.7	0.6	0.3	0.5	2.5	0.7	0.7	0.6	0.5
Sn	2.3	2.8	2.1	2.3	2.8	2.3	2.3	2.3	3.0	1.9	2.4	2.2	2.2	2.6

(Continues)

TABLE 1 (Continued)

Depth (cm)	613	621	635	638	642	648	656	670	673	680	684	687	698	705
Sb	1.6	2.1	1.4	2.0	2.5	1.9	1.8	1.8	2.2	1.1	1.9	1.7	1.6	1.9
Cs	5.5	6.0	5.0	5.0	6.0	4.6	4.7	5.2	6.4	4.1	5.3	4.8	4.6	5.6
Ba	271.4	526.1	254.1	273.7	293.5	269.4	234.4	278.7	329.2	223.6	260.7	300.3	239.4	260.6
La	31.8	36.6	29.2	34.7	39.7	35.6	31.3	31.3	40.4	26.4	36.2	35.9	37.4	39.7
Ce	60.6	71.3	56.5	66.6	75.2	74.3	57.6	61.7	80.3	55.2	74.1	78.3	81.9	80.7
Pr	7.0	8.5	6.9	8.0	8.7	9.9	6.7	7.2	9.3	6.7	8.7	9.7	10.4	9.3
Nd	25.9	31.6	26.1	29.7	31.0	41.7	24.4	27.2	35.1	25.9	32.9	38.5	42.4	35.4
Sm	4.9	6.1	5.1	5.6	5.5	8.8	4.6	5.2	6.7	5.2	6.4	7.9	9.0	7.0
Eu	1.0	1.3	1.1	1.2	1.2	1.9	1.0	1.1	1.4	1.2	1.4	1.7	2.0	1.5
Tb	0.7	0.8	0.7	0.8	0.8	1.2	0.6	0.8	0.9	0.8	0.9	1.1	1.3	1.0
Gd	4.4	5.4	4.7	5.2	5.0	8.8	4.2	4.9	6.1	5.2	6.1	7.7	8.8	6.5
Dy	4.0	4.8	4.5	4.8	4.6	6.9	3.9	4.5	5.3	4.6	5.4	6.5	7.2	5.8
Ho	0.8	1.0	0.9	1.0	1.0	1.3	0.8	0.9	1.1	1.0	1.1	1.3	1.4	1.2
Er	2.4	2.7	2.6	2.8	2.8	3.4	2.4	2.6	3.0	2.6	3.0	3.4	3.7	3.2
Tm	0.4	0.4	0.4	0.4	0.4	0.5	0.3	0.4	0.5	0.4	0.5	0.5	0.5	0.5
Yb	2.3	2.7	2.6	2.7	2.7	2.9	2.3	2.5	2.9	2.4	2.9	3.0	3.2	3.0
Lu	0.3	0.4	0.4	0.4	0.4	0.4	0.3	0.4	0.4	0.4	0.4	0.4	0.5	0.4
Hf	2.5	3.0	2.3	2.4	3.2	2.6	2.6	2.5	3.4	2.0	2.7	2.6	2.5	2.9
Ta	0.8	0.9	0.7	0.8	1.0	0.8	0.8	0.8	1.1	0.6	0.8	0.8	0.8	0.9
W	1.0	1.0	0.8	0.9	1.2	0.9	0.9	1.1	1.2	0.7	0.9	0.9	0.9	1.1
Tl	0.9	3.9	1.1	4.0	4.6	2.6	5.6	2.9	4.1	2.0	3.1	2.9	2.6	3.0
Pb	15.9	17.9	13.7	19.0	20.2	17.0	17.0	16.5	21.6	12.1	17.1	15.6	15.7	17.8
Th	8.3	9.2	7.1	8.0	9.5	8.1	8.1	8.1	10.1	6.0	8.4	8.0	8.2	9.4
U	3.7	5.8	4.0	6.0	5.8	7.6	4.9	7.2	6.3	5.9	8.2	8.6	7.0	5.0

Depth (cm)	719	722	726	729	733	740	743	761	775	785	786	787	792	796	801	805	810
Major [wt.%]																	
SiO <sub>2</sub>	31.33			36.27	39.90		32.64	31.41	40.10	16.31	5.34	5.12	1.96	1.26	0.79	0.95	4.10
TiO <sub>2</sub>	0.51			0.61	0.65		0.54	0.51	0.70	0.25	0.06	0.05	0.04	0.03	0.02	0.02	0.04
Al <sub>2</sub> O <sub>3</sub>	9.12			10.79	11.95		9.83	9.23	12.30	4.18	1.09	0.80	0.61	0.43	0.29	0.36	0.98
Fe <sub>2</sub> O <sub>3</sub>	5.64			6.95	5.48		5.67	5.82	6.37	2.15	3.05	2.98	1.71	0.67	0.58	0.98	3.40
MnO	0.04			0.04	0.04		0.05	0.05	0.04	0.10	0.21	0.26	0.18	0.09	0.08	0.16	0.26

(Continues)



TABLE 1 (Continued)

Depth (cm)	719	722	726	729	733	740	743	761	775	785	786	787	792	796	801	805	810
MgO	1.55			2.15	2.28		1.60	2.07	2.11	1.04	0.62	0.66	0.67	0.67	0.70	0.63	0.67
CaO	18.07			13.94	11.13		15.97	17.20	10.94	36.61	47.53	49.53	51.94	52.68	54.05	52.96	48.97
Na <sub>2</sub> O	0.27			0.30	0.32		0.28	0.26	0.43	0.14	0.04	0.05	0.06	0.02	0.02	0.02	0.03
K <sub>2</sub> O	1.53			1.86	2.21		1.67	1.68	2.02	0.76	0.14	0.22	0.09	0.05	0.02	0.03	0.11
P <sub>2</sub> O <sub>5</sub>	0.09			0.16	0.15		0.42	0.10	0.19	0.03	0.03	0.00	0.03	0.02	0.01	0.01	0.03
LOI	29.71			27.21	27.85		31.81	31.03	26.15	37.93	36.37	39.28	40.88	42.29	42.80	41.54	36.30
Total sum	97.9			100.3	102.0		100.5	99.3	101.4	99.5	96.85	98.94	98.16	98.21	99.36	97.66	94.89
Trace [ $\mu\text{g/g}$ ]																	
Li	28.7	24.7	29.1	38.2	37.3	38.4	44.5	41.8	29.1	19.2							
Be	2.0	1.7	2.1	2.6	2.7	2.7	3.0	3.1	2.3	1.6							
Sc	12.7	12.7	12.6	16.0	15.7	15.5	16.3	18.1	13.0	9.4							
V	210.5	173.0	187.1	221.3	227.8	309.8	379.4	303.8	207.7	130.1							
Cr	92.3	62.7	65.2	119.1	206.5	87.4	113.7	102.6	67.4	45.9							
Co	28.9	26.0	26.4	30.2	26.7	21.1	24.2	31.4	21.8	17.5							
Ni	90.5	89.2	71.1	117.0	129.5	96.5	116.4	126.9	122.4	66.2							
Cu	80.8	91.8	75.5	90.0	79.0	98.6	121.3	103.7	103.0	46.0							
Zn	151.7	162.7	159.4	114.1	97.5	127.6	225.7	90.5	66.8	36.7							
Ga	13.9	12.3	14.5	18.4	17.6	18.4	21.5	21.9	14.6	9.8							
As	86.0	15.5	31.9	23.1	76.8	18.3	22.6	27.8	18.6	12.2							
Rb	75.3	60.8	78.4	103.8	103.6	99.0	115.5	115.2	78.9	51.3							
Sr	2,422.6	3,328.7	2,578.4	816.9	643.1	739.4	564.7	611.7	547.7	542.6							
Y	31.2	30.9	30.3	33.8	32.7	44.3	44.5	35.1	61.7	34.0							
Zr	101.2	83.9	97.0	130.7	121.4	125.1	144.4	155.6	103.0	64.7							
Nb	11.8	9.7	11.2	15.9	14.8	15.0	17.7	19.5	12.9	8.2							
Mo	29.5	13.5	17.8	15.6	30.3	24.1	32.2	31.2	21.5	11.8							
Cd	0.6	0.7	0.7	0.4	0.4	0.8	1.5	0.8	0.5	0.2							
Sn	2.1	1.8	2.1	2.8	2.7	2.7	3.2	3.2	2.1	1.4							
Sb	2.2	1.3	1.6	1.9	2.3	1.7	2.3	2.1	1.5	1.8							
Cs	4.3	3.5	4.3	6.0	5.8	5.7	6.6	6.5	4.4	2.9							
Ba	228.8	212.1	222.3	275.2	260.2	385.6	325.9	335.6	240.1	152.5							
La	33.4	29.0	31.6	41.7	38.2	43.1	47.3	44.0	43.5	27.8							

(Continues)

TABLE 1 (Continued)

Depth (cm)	719	722	726	729	733	740	743	761	775	785	786	787	792	796	801	805	810
Ce	68.5	60.0	66.6	82.7	78.1	89.3	94.5	84.1	105.3	57.5							
Pr	8.3	7.3	8.1	9.6	9.2	10.8	11.3	9.5	13.7	7.0							
Nd	32.4	27.9	32.1	36.1	35.2	42.2	43.2	35.1	56.7	27.6							
Sm	6.5	5.5	6.5	7.0	7.0	8.5	8.6	6.8	12.1	5.6							
Eu	1.4	1.3	1.4	1.5	1.5	1.9	1.9	1.4	2.7	1.2							
Tb	0.9	0.9	1.0	1.0	1.0	1.3	1.3	1.0	1.8	0.9							
Gd	6.3	5.7	6.4	6.7	6.6	8.4	8.5	6.3	12.4	5.8							
Dy	5.6	5.3	5.5	6.1	5.9	7.5	7.5	5.9	10.4	5.3							
Ho	1.1	1.1	1.1	1.3	1.2	1.5	1.6	1.3	2.1	1.1							
Er	3.1	3.1	3.0	3.5	3.4	4.2	4.3	3.7	5.3	3.0							
Tm	0.5	0.5	0.4	0.5	0.5	0.6	0.6	0.6	0.7	0.4							
Yb	2.8	2.8	2.7	3.3	3.1	3.7	3.9	3.6	3.8	2.5							
Lu	0.4	0.4	0.4	0.5	0.5	0.5	0.6	0.5	0.5	0.4							
Hf	2.5	2.0	2.4	3.2	3.1	3.1	3.6	3.9	2.5	1.6							
Ta	0.8	0.6	0.7	1.0	1.0	1.0	1.1	1.3	0.8	0.5							
W	0.9	0.8	1.1	1.2	1.4	1.1	1.3	1.4	1.0	0.7							
Tl	2.4	1.8	2.5	2.0	2.1	2.0	2.9	3.4	2.0	1.4							
Pb	14.6	13.0	15.4	19.0	18.2	18.3	22.2	23.1	16.6	9.5							
Th	7.6	6.2	7.3	9.8	9.5	9.7	11.0	10.9	8.1	5.1							
U	4.1	4.9	4.3	5.4	5.5	8.5	8.8	10.3	19.1	17.2							
Depth (cm)	817	822	825	828	836	843	848	853	859	871	876	898	903	905	919	922	
Major [wt.%]																	
SiO <sub>2</sub>	25.04	35.19	36.19	34.51	35.74	34.89	34.63	30.54	31.08	33.02	32.78	36.66	39.05	35.29	37.46	33.91	
TiO <sub>2</sub>	0.43	0.59	0.61	0.60	0.60	0.59	0.57	0.50	0.53	0.55	0.55	0.60	0.72	0.60	0.66	0.57	
Al <sub>2</sub> O <sub>3</sub>	7.57	10.13	10.50	10.51	10.35	10.16	10.00	8.68	9.06	9.34	9.81	11.01	11.58	10.41	11.13	10.39	
Fe <sub>2</sub> O <sub>3</sub>	3.74	5.74	5.90	12.01	6.29	5.17	6.43	5.58	5.49	5.01	5.81	6.79	10.85	5.81	7.63	6.21	
MnO	0.07	0.04	0.04	0.04	0.05	0.04	0.04	0.04	0.04	0.05	0.05	0.04	0.04	0.04	0.05	0.04	
MgO	1.67	1.67	1.66	1.86	1.70	1.65	1.62	1.58	1.60	1.61	2.06	2.03	1.75	1.89	2.00	1.71	
CaO	22.79	13.13	12.04	6.91	13.47	14.08	13.15	16.81	14.20	16.15	15.54	11.50	7.93	11.43	10.88	12.11	
Na <sub>2</sub> O	0.22	0.33	0.36	0.32	0.33	0.34	0.32	0.28	0.29	0.30	0.30	0.35	0.36	0.34	0.32	0.32	
K <sub>2</sub> O	1.36	1.94	1.98	2.13	1.87	1.87	1.90	1.70	1.81	1.76	2.04	2.20	2.10	1.99	2.02	2.00	

(Continues)

TABLE 1 (Continued)

Depth (cm)	817	822	825	828	836	843	848	853	859	871	876	898	903	905	919	922
P <sub>2</sub> O <sub>5</sub>	0.15	0.17	0.15	0.12	0.18	0.22	0.13	0.11	0.12	0.20	0.09	0.13	0.10	0.09	0.12	0.10
LOI	34.54	32.86	31.22	31.08	29.42	31.21	32.96	35.11	32.28	25.50	30.09	29.80	25.77	31.76	31.02	32.95
Total sum	97.6	101.8	100.7	100.1	100.0	100.2	101.8	100.9	96.5	93.5	99.1	101.1	100.3	99.6	103.3	100.3
Trace [ $\mu\text{g/g}$ ]																
Li	64.9	44.3	44.3	46.2	42.2	52.8	42.5	38.0	42.1	39.1	39.4	45.1	45.2	46.5	43.3	46.7
Be	2.2	2.9	2.9	3.2	2.7	2.6	2.8	2.6	3.0	2.5	2.8	3.1	2.7	3.1	2.7	3.0
Sc	13.6	19.0	19.0	19.8	18.7	17.8	17.2	16.2	18.4	18.2	17.0	18.7	17.9	20.3	18.0	20.7
V	251.2	463.4	463.4	403.3	319.6	395.5	383.5	352.5	311.7	345.1	231.4	335.4	366.2	418.0	375.2	448.6
Cr	72.0	102.7	102.7	118.2	90.8	92.9	94.1	83.8	99.7	90.1	89.7	99.5	103.5	110.1	96.0	118.2
Co	23.9	31.2	31.2	44.9	29.5	24.3	35.4	25.7	32.7	28.7	25.3	28.4	31.3	28.4	23.5	40.1
Ni	105.6	145.3	145.3	120.6	109.4	122.1	113.5	106.6	116.2	112.8	65.1	101.5	127.7	136.5	105.1	141.1
Cu	81.4	154.9	154.9	143.7	95.6	129.9	135.6	116.1	100.4	145.7	80.3	108.6	97.0	151.0	84.9	162.0
Zn	41.1	209.8	209.8	258.1	65.1	209.2	225.3	166.2	62.1	201.4	59.1	129.4	110.8	134.6	106.9	179.8
Ga	15.5	22.7	22.7	24.1	19.3	20.7	21.2	18.7	21.2	20.1	17.8	21.8	19.9	22.0	19.9	22.4
As	16.3	23.9	23.9	57.6	26.6	20.3	47.2	23.2	24.4	20.3	33.9	29.1	59.4	23.1	34.1	27.4
Rb	79.9	116.7	116.7	129.5	106.2	105.8	112.9	99.4	113.2	100.5	108.0	122.5	114.0	119.9	112.0	119.2
Sr	571.4	709.7	709.7	562.7	1,066.9	798.8	674.7	698.2	729.7	898.5	999.2	1,042.4	910.4	800.9	409.9	639.4
Y	38.0	45.0	45.0	37.2	52.8	54.8	40.0	39.1	44.4	53.5	31.1	37.9	35.8	42.4	37.3	41.5
Zr	102.6	156.5	156.5	166.1	153.5	143.8	145.4	129.3	148.6	132.7	122.2	147.5	167.1	165.3	149.5	156.6
Nb	13.5	19.0	19.0	20.1	18.6	17.5	17.7	15.0	18.0	16.1	15.3	17.6	21.6	19.4	19.1	18.3
Mo	26.3	37.9	37.9	33.9	31.0	37.6	26.2	23.1	25.4	43.8	17.2	22.9	31.8	41.5	34.8	23.1
Cd	0.3	1.6	1.6	1.0	0.5	1.9	1.3	1.0	0.4	2.3	0.4	0.6	1.4	1.8	1.2	1.1
Sn	2.2	3.5	3.5	3.1	3.0	3.2	3.2	2.7	3.0	3.1	2.6	3.2	3.0	3.4	3.2	3.4
Sb	1.7	3.1	3.1	3.4	3.0	2.9	3.5	2.4	3.0	2.3	2.8	2.5	3.6	3.4	3.4	2.9
Cs	4.5	6.7	6.7	7.3	6.0	6.0	6.5	5.6	6.4	5.7	6.1	6.8	6.4	6.6	6.2	6.9
Ba	241.3	296.3	296.3	294.9	283.0	276.0	282.0	254.9	298.3	287.1	261.7	296.9	288.4	297.8	249.5	289.8
La	37.1	48.3	48.3	43.9	51.5	49.2	43.8	38.6	44.5	46.6	34.4	44.0	44.2	46.8	42.6	45.4
Ce	72.6	99.5	99.5	92.8	110.3	106.6	89.0	82.7	96.1	102.7	70.2	93.4	85.6	96.2	85.9	96.7
Pr	8.4	11.4	11.4	10.4	13.1	13.1	10.1	9.4	11.1	12.8	8.0	10.5	9.9	11.2	9.9	11.3
Nd	32.4	43.0	43.0	38.7	51.5	52.3	37.9	36.0	43.1	51.5	29.4	39.7	36.7	42.0	36.9	42.8
Sm	6.5	8.5	8.5	7.6	10.5	10.7	7.4	7.2	8.7	10.7	5.7	7.9	6.9	8.3	7.2	8.6
Eu	1.4	1.9	1.9	1.6	2.3	2.4	1.6	1.6	1.9	2.4	1.2	1.7	1.5	1.8	1.6	1.9

(Continues)

TABLE 1 (Continued)

Depth (cm)	817	822	825	828	836	843	848	853	859	871	876	898	903	905	919	922
Tb	1.0	1.1	1.3	1.1	1.6	1.6	1.1	1.1	1.3	1.6	0.9	1.2	1.0	1.3	1.1	1.3
Gd	6.5	7.2	8.4	7.2	10.4	10.8	7.2	7.2	8.5	10.8	5.3	7.5	6.5	8.0	6.8	8.4
Dy	6.0	6.8	7.8	6.8	9.3	9.5	6.9	6.8	7.8	9.4	5.4	6.9	6.3	7.6	6.5	7.8
Ho	1.3	1.4	1.6	1.4	1.9	2.0	1.5	1.4	1.6	1.9	1.2	1.5	1.4	1.6	1.4	1.6
Er	3.6	4.2	4.6	4.2	5.2	5.2	4.2	4.1	4.5	5.1	3.4	4.1	3.9	4.7	4.0	4.6
Tm	0.5	0.6	0.7	0.6	0.7	0.7	0.6	0.6	0.7	0.7	0.5	0.6	0.6	0.7	0.6	0.7
Yb	3.3	4.1	4.5	4.1	4.7	4.6	4.0	3.9	4.3	4.4	3.4	3.9	3.9	4.6	4.0	4.5
Lu	0.5	0.6	0.7	0.6	0.7	0.7	0.6	0.6	0.6	0.6	0.5	0.6	0.6	0.7	0.6	0.7
Hf	2.6	4.2	3.9	4.2	4.0	3.6	3.7	3.2	3.7	3.3	3.3	3.8	4.4	4.2	4.0	4.0
Ta	0.9	1.3	1.3	1.3	1.2	1.2	1.2	1.0	1.2	1.1	1.0	1.2	1.4	1.3	1.3	1.2
W	5.9	11.9	1.3	11.9	1.6	9.5	1.2	1.1	8.4	7.4	6.5	1.3	1.4	7.6	1.3	6.0
Tl	1.9	5.0	3.5	5.0	3.0	2.9	3.4	2.9	2.8	2.5	2.9	2.9	4.1	4.5	3.0	5.5
Pb	14.9	25.6	25.6	26.0	20.4	22.8	24.4	19.5	20.2	21.1	20.6	21.5	33.3	32.4	22.9	37.4
Th	7.8	11.4	11.4	11.4	11.0	10.5	10.3	9.2	10.7	10.0	9.1	11.1	11.1	11.3	10.4	11.3
U	13.0	8.2	8.2	7.4	8.3	9.1	7.0	7.1	8.5	8.8	4.4	6.2	6.1	9.2	6.8	7.4
Depth (cm)	940	949	956	964	971	976	986	1,003	1,009	1,020	1,030	1,040	1,050			
SiO <sub>2</sub>	33.24	41.90	31.73	43.12	19.18	23.36	35.00	37.37	38.94	36.50	36.40	37.33	36.13			
TiO <sub>2</sub>	0.58	0.72	0.51	0.81	0.30	0.32	0.55	0.62	0.67	0.64	0.61	0.62	0.61			
Al <sub>2</sub> O <sub>3</sub>	10.25	12.69	9.86	13.11	6.30	6.51	11.04	12.36	13.19	12.37	12.13	12.61	12.14			
Fe <sub>2</sub> O <sub>3</sub>	12.58	6.18	5.15	6.23	3.79	3.73	9.37	3.50	4.30	4.09	4.15	4.04	3.92			
MnO	0.04	0.04	0.05	0.04	0.07	0.10	0.06	0.15	0.13	0.13	0.16	0.15	0.15			
MgO	2.07	2.32	1.69	2.39	1.18	1.34	1.76	2.27	2.33	2.43	2.53	2.59	2.49			
CaO	9.45	7.31	16.79	7.42	26.29	27.27	11.83	18.88	16.59	18.80	18.85	18.68	18.89			
Na <sub>2</sub> O	0.34	0.43	0.31	0.45	0.20	0.22	0.38	0.42	0.45	0.43	0.43	0.43	0.42			
K <sub>2</sub> O	2.10	2.52	1.91	2.65	1.20	1.25	2.23	2.56	2.74	2.58	2.54	2.65	2.46			
P <sub>2</sub> O <sub>5</sub>	0.10	0.13	0.12	0.10	0.13	0.12	0.11	0.13	0.13	0.11	0.14	0.15	0.16			
LOI	28.97	25.15	31.37	23.82	36.93	30.45	28.19	23.62	20.58	21.18	21.85	21.50	21.60			
Total sum	99.7	99.4	99.5	100.1	95.6	94.7	100.5	101.9	100.1	99.3	99.8	100.8	99.0			
Trace [ $\mu\text{g/g}$ ]																
Li	41.7	52.9	43.1	51.7	30.8	27.1	50.6	46.0	49.7	43.7	43.2	44.4	44.7			
Be	2.8	3.4	2.6	3.3	1.9	1.6	2.8	2.3	2.7	2.4	2.3	2.3	2.3			

(Continues)

TABLE 1 (Continued)

Depth (cm)	940	949	956	964	971	976	986	1,003	1,009	1,020	1,030	1,040	1,050
Sc	18.5	21.7	20.7	20.5	18.7	15.0	21.3	18.5	19.4	17.8	17.5	17.9	18.0
V	325.3	381.5	330.2	413.2	266.0	215.4	164.7	121.8	132.0	110.4	110.4	103.9	99.2
Cr	97.6	126.1	101.4	127.0	75.8	69.6	109.2	80.8	87.5	76.3	75.6	75.9	76.0
Co	40.1	30.7	34.6	30.8	37.4	33.1	106.9	17.4	23.7	21.2	20.6	19.1	23.7
Ni	123.3	112.9	115.8	149.6	279.7	192.6	224.3	70.8	84.0	74.1	73.6	68.5	70.2
Cu	115.4	136.2	127.9	123.6	129.8	104.8	115.5	35.6	47.8	37.2	35.7	36.0	32.4
Zn	124.5	143.9	123.1	105.8	320.4	476.2	81.7	148.3	192.1	150.7	106.4	140.4	85.9
Ga	19.7	25.3	19.1	23.5	14.6	12.2	20.3	17.4	19.1	17.1	16.6	16.7	16.4
As	85.8	21.0	20.7	22.5	22.8	21.8	67.4	10.0	13.9	11.0	10.5	11.2	9.9
Rb	113.9	140.7	107.0	138.9	70.4	63.3	117.1	108.5	118.2	106.7	106.6	107.2	105.9
Sr	551.5	413.5	833.8	510.1	2,750.1	1,503.5	871.0	1,766.0	1,782.2	1,341.5	1,107.9	1,028.8	1,128.9
Y	34.7	41.0	48.3	32.8	61.1	55.6	34.8	34.3	32.3	27.8	31.9	33.0	35.1
Zr	137.7	172.7	120.9	184.3	87.2	73.2	111.1	98.8	115.3	99.5	95.4	95.2	97.5
Nb	17.7	22.2	14.7	24.5	9.1	8.2	14.4	13.7	14.8	13.7	13.3	13.2	13.1
Mo	36.8	26.5	15.1	27.1	24.8	17.4	4.5	1.3	2.0	1.3	0.9	1.0	1.2
Cd	0.6	1.2	0.7	1.2	2.4	3.4	0.1	0.2	0.3	0.2	0.1	0.2	0.1
Sn	3.1	3.9	3.0	3.9	2.0	2.1	3.5	3.0	3.2	2.8	2.8	2.8	2.7
Sb	3.0	3.6	2.2	3.3	1.9	1.3	3.6	0.8	1.2	1.0	0.8	0.8	0.7
Cs	6.4	7.8	6.3	7.7	4.3	3.7	7.0	6.4	7.1	6.4	6.3	6.4	6.3
Ba	324.0	338.5	280.4	333.3	219.1	187.0	353.4	321.7	354.5	311.5	321.0	319.6	308.9
La	39.0	47.6	46.0	44.2	43.1	34.8	48.0	42.5	47.1	41.7	38.7	38.8	41.2
Ce	85.8	103.3	106.9	88.3	102.6	78.3	96.4	86.2	95.4	84.9	78.6	79.0	84.0
Pr	9.8	12.2	13.3	10.0	14.0	10.8	10.9	10.4	11.2	9.9	9.6	9.9	10.7
Nd	37.3	47.2	54.0	35.0	61.0	48.2	40.3	39.5	40.6	35.4	36.6	38.4	42.1
Sm	7.4	9.6	11.7	6.3	13.7	11.3	7.7	7.7	7.3	6.4	7.5	8.1	8.8
Eu	1.6	2.0	2.5	1.3	3.2	2.6	1.6	1.7	1.6	1.3	1.6	1.7	1.9
Tb	1.1	1.4	1.7	0.9	2.0	1.7	1.1	1.1	1.0	0.9	1.0	1.1	1.2
Gd	7.1	8.9	11.1	5.6	13.9	11.6	7.0	7.2	6.5	5.5	6.8	7.3	8.1
Dy	6.5	7.8	9.4	5.8	11.2	9.8	6.4	6.3	5.9	5.1	5.9	6.2	6.8
Ho	1.4	1.6	1.9	1.3	2.2	2.0	1.3	1.3	1.2	1.1	1.2	1.3	1.3
Er	3.8	4.4	4.9	3.8	5.4	5.0	3.7	3.5	3.4	3.0	3.3	3.4	3.5
Tm	0.6	0.7	0.7	0.6	0.7	0.7	0.6	0.5	0.5	0.5	0.5	0.5	0.5

(Continues)

TABLE 1 (Continued)

Depth (cm)	940	949	956	964	971	976	986	1,003	1,009	1,020	1,030	1,040	1,050
Yb	3.7	4.2	4.3	3.9	4.4	4.0	3.5	3.3	3.3	2.9	3.0	3.1	3.2
Lu	0.5	0.6	0.6	0.6	0.6	0.6	0.5	0.5	0.5	0.4	0.4	0.4	0.5
Hf	3.6	4.5	3.2	4.8	2.1	1.8	3.1	2.8	3.2	2.8	2.7	2.8	2.8
Ta	1.1	1.5	1.0	1.6	0.6	0.5	1.0	0.9	1.0	0.9	0.9	0.9	0.9
W	1.1	7.7	7.2	7.0	4.1	5.1	6.0	1.8	1.8	1.3	1.1	1.0	1.0
Tl	3.8	3.6	3.6	5.8	6.4	5.5	2.0	0.5	0.7	0.6	0.6	0.6	0.6
Pb	71.1	58.8	60.5	79.5	72.2	45.7	73.2	21.0	26.4	22.1	21.2	21.8	21.6
Th	10.0	12.4	9.9	12.8	7.1	5.8	10.4	9.3	10.6	9.7	9.5	9.5	9.6
U	6.2	7.6	9.3	6.3	13.3	9.3	4.3	3.3	3.5	2.7	2.9	3.0	3.0

## 4.2 | TOC<sub>cf</sub>, carbonate and isotopic data

The TOC<sub>cf</sub> contents and bulk stable isotope (carbon and oxygen) data are given in Table 2 and are plotted in Figures 6 and 7. Carbonate concentrations are reported in Table 2. The gray bioturbated mudstone samples have lower TOC<sub>cf</sub> contents <5 wt.% than laminated oil shales with consistently TOC<sub>cf</sub> contents >5 wt.% (Table 2, Figure 6). Unterer Stein shows high carbonate contents with an average of 92 wt%, the rest of this studied samples exhibit a variation between 3 to 88 wt%. According to the distribution of organic-rich sediments in the Dotternhausen section, this study places the onset of the Toarcian OAE to a depth of 980 cm in our profile. Four data points at depths between 1,012 cm and 986 cm reveal constant  $\delta^{13}\text{C}_{\text{carb}}$  and  $\delta^{13}\text{C}_{\text{org}}$  values prior to the Toarcian OAE (Figure 7). The negative  $\delta^{13}\text{C}_{\text{carb}}$  and  $\delta^{13}\text{C}_{\text{org}}$  excursions ranging from 0 to -12‰ and -28 to -32‰, respectively, are exhibited between depths of 986 cm and 613 cm (Figure 7). Two-step opposing small-scale excursions of  $\delta^{13}\text{C}_{\text{carb}}$  and  $\delta^{13}\text{C}_{\text{org}}$  records from 876 to 761 cm are obviously observed (Figure 7). The  $\delta^{13}\text{C}_{\text{carb}}$  values in the first and smaller scale (from 876 to 825 cm) has a negative excursion, which corresponds to a slightly positive excursion in  $\delta^{13}\text{C}_{\text{org}}$  values. By contrast, the second step (from 825 to 761 cm) has larger magnitude excursions in both  $\delta^{13}\text{C}_{\text{carb}}$  and  $\delta^{13}\text{C}_{\text{org}}$  values (Figure 7). The  $\Delta^{13}\text{C}$  ( $\delta^{13}\text{C}_{\text{carb}} - \delta^{13}\text{C}_{\text{org}}$ ) is relatively constant in the lower part (interval 1 from 981 to 883 cm) and upper part (interval 3 from 757 to 613 cm), whereas it drops according to the two-step opposing small-scale excursions (interval 2 from 876 to 761 cm; Figure 7). The  $\delta^{18}\text{O}$  values of carbonates range from -7 to -4‰, and the heaviest values are preserved in the diagenetically lenticular limestone bed of Unterer Stein (Figure 7).

## 5 | DISCUSSION

### 5.1 | Negligible effects of terrigenous-sourced organic carbon, thermal maturity, and hydrothermal fluids on $\delta^{13}\text{C}_{\text{org}}$ across the Toarcian CIE

Due to the contrasting  $\delta^{13}\text{C}$  signatures between terrestrial and marine organic matters, terrestrial-sourced organic carbon can lead to a significant influence on  $\delta^{13}\text{C}_{\text{org}}$  record of marine sediments deposited across the Toarcian CIE (Suan et al., 2015). Indeed, decomposed organic material from land plants can be easily washed into shelf-sea settings as a result of an accelerated hydrological cycle (Izumi, Kemp, Itamiya, & Inui, 2018) arising from the intensive chemical weathering (e.g., Cohen, Coe, Harding, & Schwark, 2004; Percival et al., 2016). Hydrogen index (HI) is an efficient indicator that can distinguish between marine and terrestrial organic matter (e.g., Dembicki, 2009; Peters, Walters, & Moldowan, 2005). In general, a HI value higher than 400 mg hydrocarbon (HC)/g TOC indicates the preservation of oil-prone marine organic matter (types I and II kerogen) dominated by algae and bacteria (Röhl, Schmid-Röhl, Oschmann, Frimmel, & Schwark, 2001). Although the use of HI in characterizing the type of

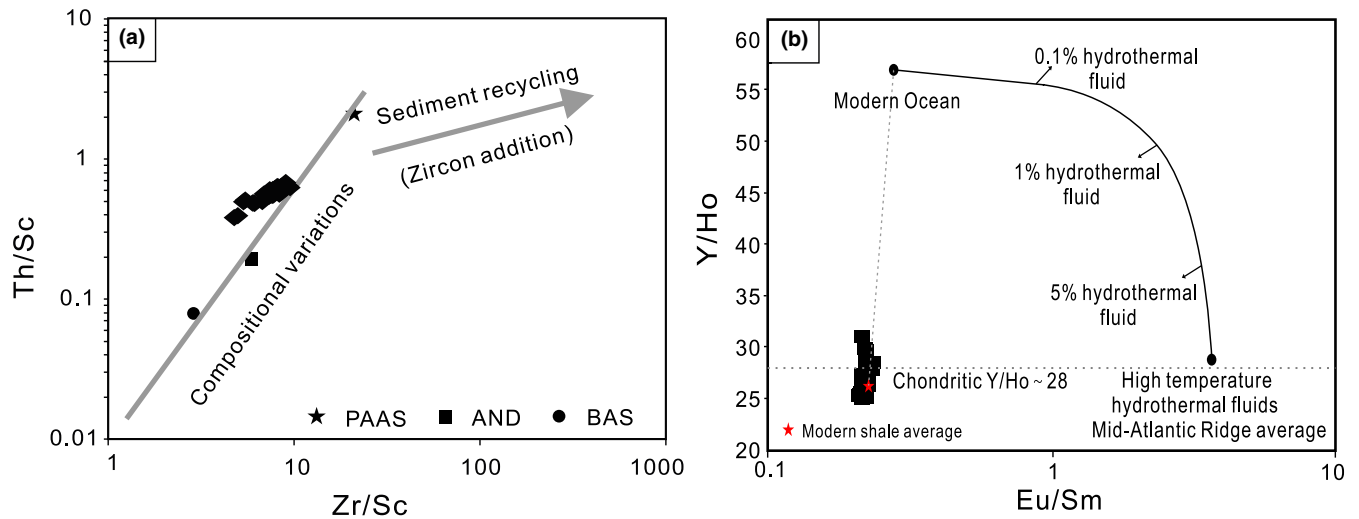


**FIGURE 4** (a) Th/Sc vs. Zr/Sc diagram (McLennan, Hemming, McDaniel, & Hanson, 1993). AND, andesite; BAS, basalt; PAAS, post-Archean Australian shale; (b) Y/Ho vs. Eu/Sm diagram (modified from Albut et al., 2018, and references therein)

kerogen is not straightforward, because high thermal volatilization can considerably contribute to lower this index (Dembicki, 2009; de Kock et al., 2017), the Dotternhausen black shale and limestone beds exhibit relatively invariable HI values of ~580 mg HC/g TOC and

high  $\text{TOC}_{cf}$  contents of ~13 wt.% (Figure 6). This demonstrates that the organic matter was well preserved and of predominantly marine origin—here, bolstered by the oil shale character of the studied section (Röhl, Schmid-Röhl, Oschmann, Frimmel, & Schwark, 2001).

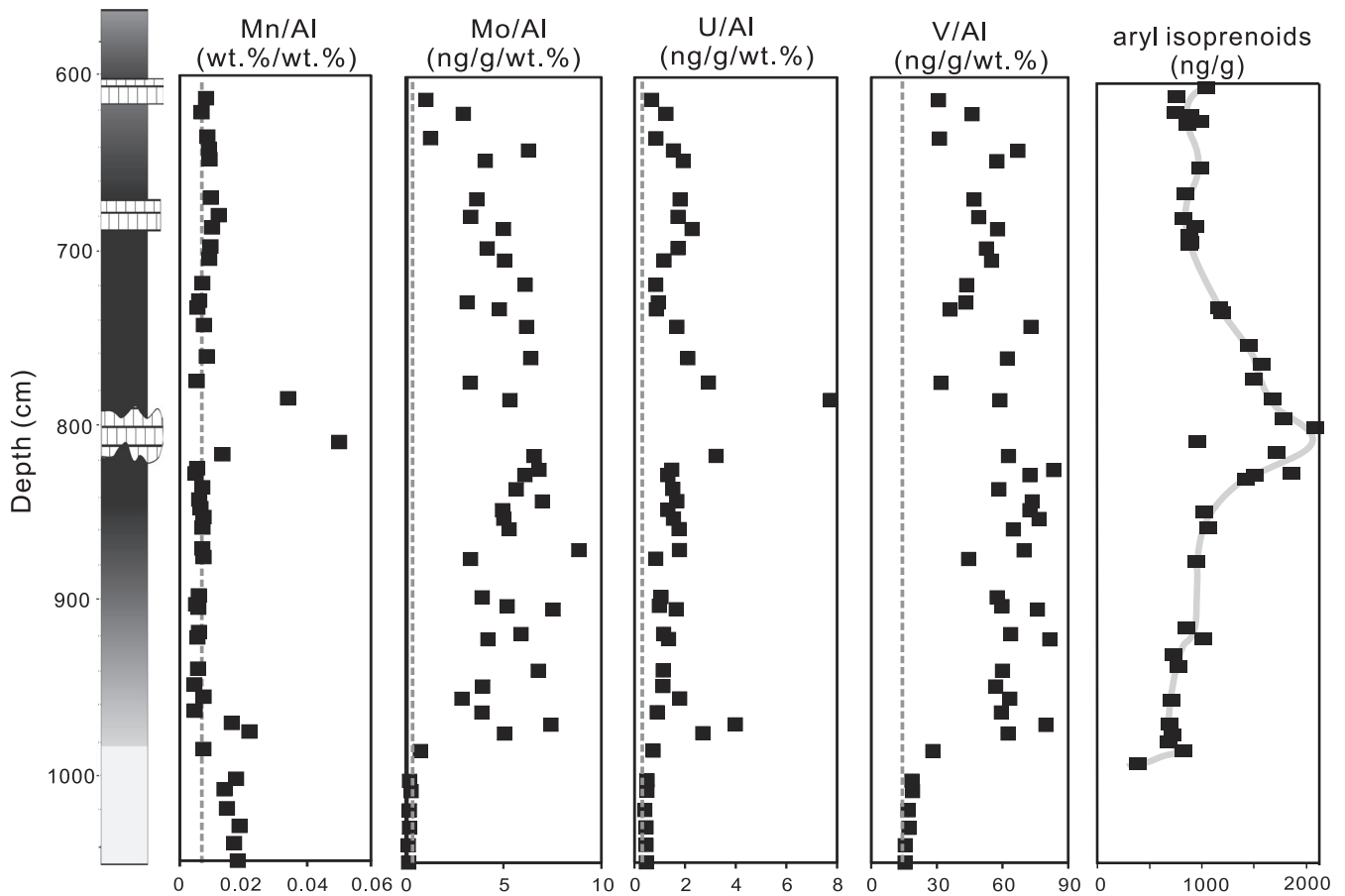


**FIGURE 5** Stratigraphic profiles of Mn, Mo, U and V enrichments in the Dotternhausen section. Stratigraphic distribution of aryl isoprenoid (GSB biomarker) abundance is from Schwark & Frimmel (2004). Dashed lines denote the according reference values of upper continental crust (UCC; McLennan, 2001)

**TABLE 2** Stable isotope and TOC<sub>cf</sub> carbonate data for Dotternhausen samples

Depth [cm]	$\delta^{13}\text{C}_{\text{carb}}$ [‰] VPDB	$\delta^{13}\text{C}_{\text{org}}$ [‰] VPDB	$\Delta^{13}\text{C}_{\text{carb-}}$ $\text{org}$ [‰] VPDB	$\delta^{18}\text{O}$ [‰] VPDB	TOC <sub>cf</sub> [wt.%]	CaCO <sub>3</sub> [wt.%]	[DIC] <sub>total</sub> [wt.%]	[DIC] <sub>org</sub> [wt.%]	[DIC] <sub>org</sub> / [DIC] <sub>total</sub> [%]
613	0.38	-26.94	27.32	-5.65	3.9	29.79	3.57	—	—
616	0.19	-27.32	27.51	-5.99	7.6	44.76	5.37	—	—
621	0.09	-27.12	27.21	-5.77	10.3	8.61	1.03	0.00	0
624	-0.4	-27.87	27.47	-6.32	7.9	43.94	5.27	0.08	1
628	-0.08	-27.43	27.35	-6.28	7.0	39.86	4.78	0.01	0
631	-0.06	-27.42	27.37	-5.92	7.0	29.68	3.56	0.01	0
635	-0.19	-27.11	26.92	-5.44	5.4	44.32	5.32	0.04	1
638	-0.44	-27.52	27.08	-6.34	8.9	40.16	4.82	0.08	2
642	-0.74	-28.09	27.35	-6.01	7.4	29.24	3.51	0.09	3
645	-0.77	-27.12	26.35	-6.67	11.0	65.54	7.86	0.22	3
648	-0.45	-27.74	27.28	-6.54	12.8	29.03	3.48	0.06	2
652	-0.64	-29.05	28.41	-6.69	7.5	56.48	6.78	0.15	2
656	-0.47	-28.87	28.41	-6.34	8.8	41.47	4.98	0.08	2
670	-0.93	-27.32	26.39	-6.19	12.7	31.73	3.81	0.13	3
673	-0.77	-28.66	27.89	-6.35	9.2	28.2	3.38	0.09	3
677	-0.67	-28.07	27.4	-6.04	6.8	58.63	7.04	0.17	2
680	-0.62	-28.26	27.64	-6	7.4	56.25	6.75	0.15	2
684	-1.01	-28.69	27.68	-6.25	10.1	37.75	4.53	0.16	4
687	-1.12	-27.9	26.78	-6.22	9.5	42.99	5.16	0.21	4
691	-0.97	-28.51	27.54	-6.54	11.2	32.62	3.91	0.13	3
694	-1.62	-30.37	28.75	-6.69	8.8	49.81	5.98	0.32	5
698	-1.54	-29.25	27.71	-6.48	14.6	3.47	0.42	0.02	5
701	-1.7	-29.68	27.98	-6.56	10.7	42.86	5.14	0.29	6
705	-1.38	-30.03	28.65	-6.38	8.1	31.96	3.84	0.18	5
708	-1.55	-29.79	28.24	-5.99	5.5	24.86	2.98	0.16	5
712	-1.33	-29.76	28.43	-6.16	6.2	48.94	5.87	0.26	4
715	-1.78	-29.17	27.39	-6.6	10.3	43.79	5.25	0.32	6
719	-1.49	-29.8	28.32	-6.34	8.1	36.63	4.40	0.22	5
722	-1.64	-29.76	28.12	-6.68	10.7	53.12	6.37	0.35	6
726	-2.43	-30.92	28.49	-6.15	9.8	36.32	4.36	0.34	8
729	-2.24	-30.25	28.01	-6.11	7.5	36.84	4.42	0.33	7
733	-2.53	-30.35	27.82	-5.71	5.8	29.11	3.49	0.29	8
736	-3.12	-31.44	28.32	-6.44	10.8	87.92	10.55	1.05	10
740	-2.37	-31.28	28.91	-6.73	11.9	24.88	2.99	0.23	8
743	-2.61	-31.38	28.77	-6.59	11.8	24.69	2.96	0.25	8
747	-2.46	-30.34	27.88	-6.56	10.8	36.91	4.43	0.36	8
750	-2.93	-31.34	28.42	-6.57	11.8	25.3	3.04	0.28	9
754	-3.23	-31.22	27.99	-6.54	15.1	32.59	3.91	0.40	10
757	-2.62	-31.83	29.22	-6.37	9.4	25.5	3.06	0.25	8
761	-3.57	-31.28	27.71	-6.02	12.1	29.08	3.49	0.40	11
764	-3.3	-31.03	27.72	-6.39	14.0	25.04	3.00	0.32	11
768	-4.64	-30.33	25.69	-6.91	6.7	52.69	6.32	0.97	15
771	-5.21	-30.68	25.47	-6.64	8.2	54.45	6.53	1.11	17

(Continues)



TABLE 2 (Continued)

Depth [cm]	$\delta^{13}\text{C}_{\text{carb}}$ [‰] VPDB	$\delta^{13}\text{C}_{\text{org}}$ [‰] VPDB	$\Delta^{13}\text{C}_{\text{carb-}}$ $\text{org}$ [‰] VPDB	$\delta^{18}\text{O}$ [‰] VPDB	TOC <sub>cf</sub> [wt.%]	CaCO <sub>3</sub> [wt.%]	[DIC] <sub>total</sub> [wt.%]	[DIC] <sub>org</sub> [wt.%]	[DIC] <sub>org</sub> / [DIC] <sub>total</sub> [%]
775	-3.9	-30.22	26.32	-7.18	8.5	42.64	5.12	0.66	13
778	-4.26	-30.25	25.99	-6.97	7.5	50.9	6.11	0.86	14
781	-6.52	-31.8	25.27	-7.05	10.5	33.54	4.02	0.83	21
785	-5.99	-30.56	24.57	-6.55	7.2	67.14	8.06	1.58	20
788	-5.89	-30.75	24.86	-5.11		81.99	9.84	1.88	19
796	-12.6	-30.11	17.51	-4.17		95.05	11.41	4.77	42
801	-12.17	-28.76	16.59	-4.19		87.79	10.53	4.46	42
805	-11.27	-29.75	18.48	-4.69		92.57	11.11	4.21	38
815	-5.89	-31.15	25.26	-5.63		83.4	10.01	1.89	19
817	-5.92	-31.77	25.85	-6.34	11.0	48.61	5.83	1.09	19
822	-6.19	-32.37	26.18	-6.48	11.9	24.48	2.94	0.56	19
825	-6.27	-32.15	25.88	-6.54	11.7	21.27	2.55	0.50	20
828	-4.95	-31.93	26.97	-6.74	12.5	13.37	1.60	0.25	16
831	-5.34	-32.26	26.92	-6.43	13.1	14.81	1.78	0.29	17
834	-5.66	-31.96	26.3	-6.44	13.3	19.04	2.28	0.40	18
836	-7.21	-33.2	25.99	-6.19	10.7	23.95	2.87	0.62	22
840	-6.23	-32.36	26.13	-7.1	11.5	35.83	4.30	0.83	19
843	-6.6	-31.79	25.19	-6.23	11.8	22.18	2.66	0.55	21
848	-6.79	-32.09	25.3	-6.76	11.6	23.16	2.78	0.59	21
850	-8.82	-31.94	23.12	-5.5	11.3	41.24	4.95	1.37	28
853	-7.83	-32.15	24.32	-6.59	12.0	29.84	3.58	0.87	24
856	-7.24	-32.23	24.99	-6.38	13.4	26.44	3.17	0.71	22
859	-7.57	-32.51	24.94	-5.55	15.9	22.47	2.70	0.63	23
862	-5.92	-32.44	26.52	-6.29	9.0	18.97	2.28	0.42	18
869	-5.5	-32.22	26.72	-6.16	5.5	17.01	2.04	0.35	17
869	-6.6	-32.39	25.79	-6.49	12.0	23.58	2.83	0.58	20
871	-5.14	-31.79	26.66	-5.83	12.4	28.36	3.40	0.55	16
876	-4.23	-31.64	27.41	-5.45	9.6	28.61	3.43	0.46	13
883	-4.53	-31.89	27.36	-6.52	14.4	18.91	2.27	0.32	14
894	-6.09	-32.3	26.21	-6.13	14.7	20.83	2.50	0.47	19
898	-5.55	-32.28	26.73	-6.73	10.1	20.81	2.50	0.43	17
899	-5.62	-32.23	26.61	-6.51	10.9	16.18	1.94	0.34	17
903	-4.71	-32.92	28.21	-6.91	7.2	13.99	1.68	0.24	14
905	-5.17	-31.98	26.82	-6.04	12.9	23.07	2.77	0.45	16
914	-5.53	-31.5	25.97	-6.59	14.1	19.69	2.36	0.41	18
917	-5.52	-31.37	25.86	-6.78	13.3	23.59	2.83	0.50	18
919	-6.23	-33.27	27.04	-6.51	6.1	19.31	2.32	0.43	19
921	-3.93	-30.83	26.9	-6.43	12.8	21.22	2.55	0.32	13
922	-3.1	-30.8	27.7	-6.28	13.0	24.4	2.93	0.29	10
926	-4.12	-30.96	26.84	-6.28	11.8	23.23	2.79	0.37	13
935	-4	-30.98	26.98	-6.13	12.8	24.56	2.95	0.38	13
940	-4.03	-32.08	28.05	-6.22	8.2	18.06	2.17	0.27	13
949	-3.47	-31.7	28.23	-6.41	9.8	15.18	1.82	0.20	11

(Continues)

TABLE 2 (Continued)

Depth [cm]	$\delta^{13}\text{C}_{\text{carb}}$ [‰] VPDB	$\delta^{13}\text{C}_{\text{org}}$ [‰] VPDB	$\Delta^{13}\text{C}_{\text{carb-org}}$ [‰] VPDB	$\delta^{18}\text{O}$ [‰] VPDB	TOC <sub>cf</sub> [wt.%]	CaCO <sub>3</sub> [wt.%]	[DIC] <sub>total</sub> [wt.%]	[DIC] <sub>org</sub> [wt.%]	[DIC] <sub>org</sub> / [DIC] <sub>total</sub> [%]
956	-3.26	-30.36	27.1	-6.43	9.9	34.48	4.14	0.44	11
961	-3.23	-31.01	27.78	-6.12	7.7	18.44	2.21	0.23	10
964	-2.73	-31.34	28.61	-6.08	8.7	14.38	1.73	0.15	9
971	-1.64	-28.15	26.51	-6.21	12.6	51.81	6.22	0.36	6
976	-2	-29.02	27.01	-6.06	8.2	49.93	5.99	0.41	7
979	-1.71	-29.64	27.93	-6.36	4.6	22.09	2.65	0.15	6
981	-0.69	-27.27	26.57	-6.99	1.8	17.65	2.12	0.05	3
986	-1.11	-28.91	27.8	-6.47	8.0	22.78	2.73	0.10	4
993	-1.05	-27.24	26.19	-6.7	2.7	25.43	3.05	0.12	4
993	-1.15	-27.66	26.51	-6.67	3.0	27.82	3.34	0.14	4
1,003	-1.18	-26.65	25.47	-5.87	0.8	35.73	4.29	0.19	4
1,012	-0.89	-27.88	26.99	-5.71	3.1	28.8	3.46	0.11	3

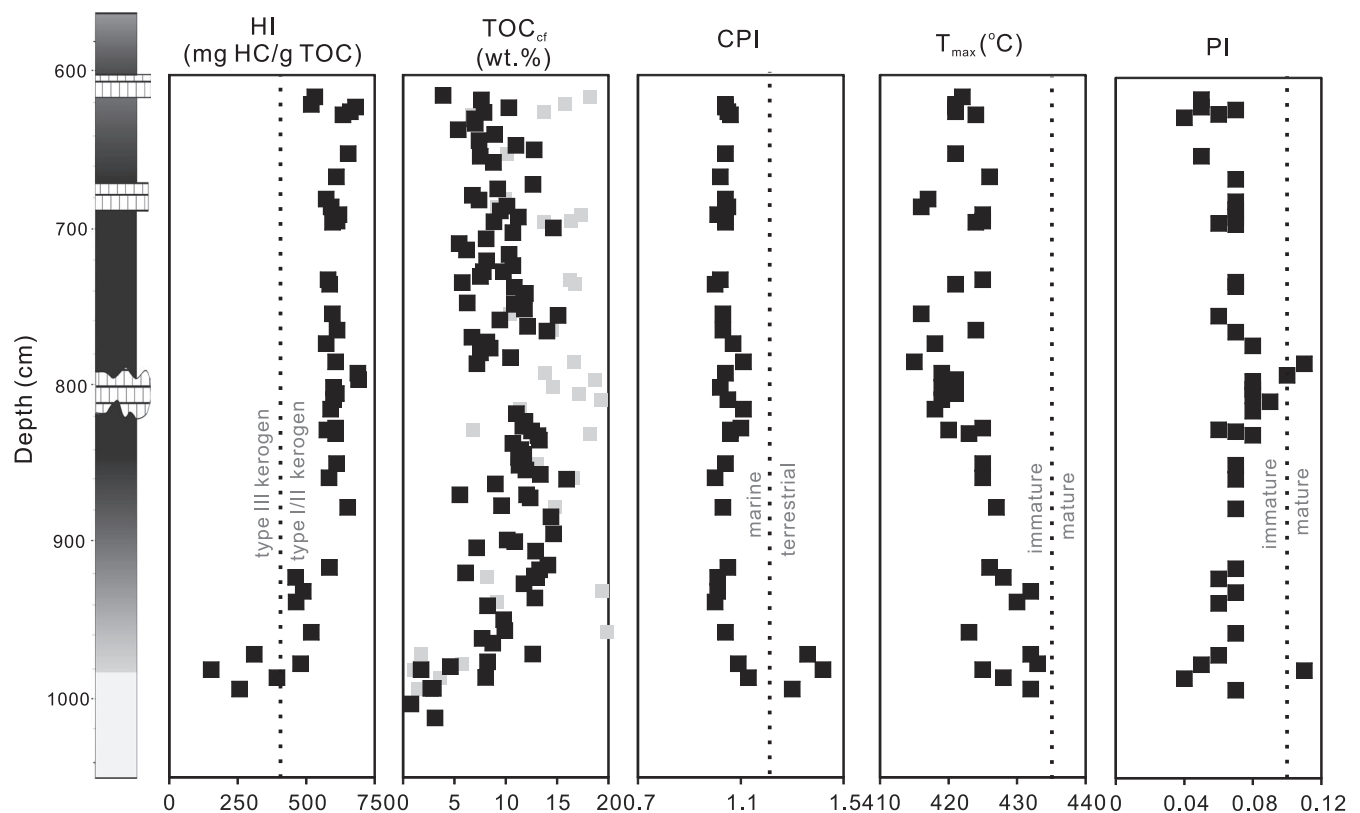


**FIGURE 6** Rock-Eval pyrolysis data of the Dotternhausen sedimentary section. The HI, CPI,  $T_{\text{max}}$ , PI, and TOC<sub>cf</sub> of gray rectangles are from Frimmel, Oschmann, & Schwark (2004)

The carbon preference index (CPI) with relatively low values of ~1 in the Dotternhausen black shale sediments (Figure 6) further implies low contribution from terrestrial-derived organic matter (CPI >1.2: Ruebsam, Müller, Kovács, Pálffy, & Schwark, 2018).

The  $\delta^{13}\text{C}_{\text{org}}$  signals in the Dotternhausen black shales can also be perturbed by recycled sediments from organic matter-rich

catchment areas. Such recycled organic matter is generally marked by high thermal maturity that can alter the primarily preserved organic carbon isotope signals. To assess the possible contamination from recycled organic matters on the Dotternhausen black shales, we here refer to molecular maturity indicators such as Rock-Eval  $T_{\text{max}}$  (°C) and production index (PI) published in previous studies

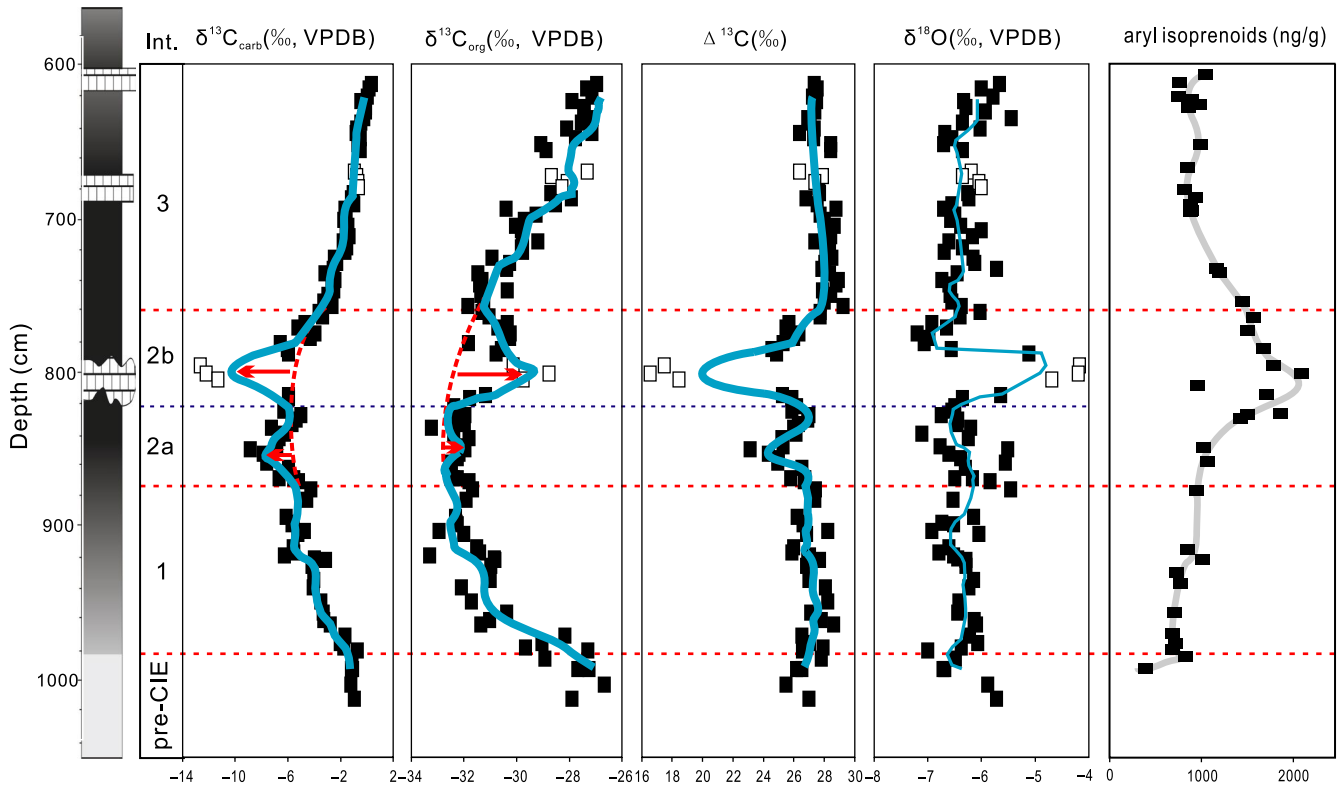


**FIGURE 7** Stratigraphic profiles of  $\delta^{13}\text{C}_{\text{carb}}$ ,  $\delta^{13}\text{C}_{\text{org}}$ ,  $\Delta^{13}\text{C}$  ( $\Delta^{13}\text{C} = \delta^{13}\text{C}_{\text{carb}} - \delta^{13}\text{C}_{\text{org}}$ ) and  $\delta^{18}\text{O}$  in the Dotternhausen section. Stratigraphic distributions of aryl isoprenoid (GSB biomarker) abundance are from Schwark & Frimmel (2004). The red dashed arcs denote the theoretic Toarcian CIE curves without suffering local-scale carbon-cycle perturbations. The blue lines represent the 5-point moving average of the isotopic data. Int.: interval. White rectangles particularly represent the isotopic data from limestone beds

(cf. Frimmel, 2003; Frimmel, Oschmann, & Schwark, 2004). The  $T_{\text{max}}$  values (mean = 427°C) without any considerable variation (Figure 6) together with high HI demonstrate that the organic matter in Dotternhausen black shale is neither overmature nor inert. This demonstrates the lack of significant contamination with recycled sediments. The possibility of sedimentary recycling can also be traced by inorganic proxies. For instance, recycled sediments would display a substantial increase in Zr/Sc along with a much smaller magnitude increase in Th/Sc (McLennan, Hemming, McDaniel, & Hanson, 1993). A crossplot of Zr/Sc versus Th/Sc was adopted to track possible recycling processes on the studied black shale samples (McLennan, Hemming, McDaniel, & Hanson, 1993). Though the data show a slight deviation from the compositional variation trend indicative for single cycling from parent rock material, all their Zr/Sc ratios (<10) (Figure 4a) are low and comparable to that of pristine provenance rocks, indirectly revealing the minimal influence from polycyclic reworking of sedimentary rocks. In addition, hydrothermal fluid can preferentially liberate  $^{12}\text{C}$  and introduce external hydrocarbon into organic-rich sedimentary rocks, which would influence their pristine  $\delta^{13}\text{C}_{\text{org}}$  values (Jiang et al., 2012; Pinti, Hashizume, Sugihara, Massault, & Philippot, 2009). The influence of high-temperature fluids on sediments can be tested in a crossplot between Y/Ho and Eu/Sm (Figure 4b; cf. Albut et al., 2018, and references therein). The Dotternhausen black shales exhibit chondritic Y/Ho

ratios (~28) similar to the modern shale average (Albut et al., 2018, and references therein). Yttrium is less effectively scavenged from seawater than the trivalent REE Ho, leading to high residual Y/Ho ratios in the oceans. High-temperature hydrothermal fluids are also characterized by chondritic Y/Ho ratios, but exhibit higher Eu/Sm ratios than oceanic or continental crust due to the higher solubility of reduced divalent Eu compared to trivalent Sm. The Dotternhausen black shales have Eu/Sm ratios of 0.21 and 0.23, which are within the range of the modern shale average, but an order of magnitude lower than typical high-temperature hydrothermal fluids at mid-ocean ridges (Figure 4b). This observation demonstrates negligible alteration by hydrothermal activity on the studied black shale facies. In summary, the  $\delta^{13}\text{C}_{\text{org}}$  records of Dotternhausen Toarcian CIE samples were not significantly influenced by terrigenous-derived organic matters, contaminated by recycling of old sediments, and altered by hydrothermal activity.

## 5.2 | Marine redox condition record in the Dotternhausen succession during the Toarcian CIE

During the Toarcian CIE high rates of organic carbon production occurred in the proximal shelf areas of the northwestern part of Tethys margin (e.g., French et al., 2014; Frimmel, Oschmann, & Schwark,

2004; Schwark & Frimmel, 2004). These were commonly tied to high marine productivity rates (e.g., Jenkyns, 2010; Röhl, Schmid-Röhl, Oschmann, Frimmel, & Schwark, 2001) caused by excessive nutrient input from enhanced continental weathering (e.g., Cohen, Coe, Harding, & Schwark, 2004; Percival et al., 2016). It was proposed that the generated organic matter subsequently suffered aerobic degradation during which the seawater oxygen inventory was massively depleted (Röhl, Schmid-Röhl, Oschmann, Frimmel, & Schwark, 2001). Furthermore, at a high sea-level stand during the Toarcian CIE period (Ruebsam, Mayer, & Schwark, 2019), the strong water-column stratification and hydrological restriction have prevented efficient ventilation between bottom waters and the outside open ocean, which eventually promoted the formation of anoxic benthic seawaters in the northwestern Tethys shelf-sea settings (e.g., Guillaume and Yannick, 2012; Hermoso et al., 2013; McArthur et al., 2008; Ruvalcaba Baroni et al., 2018; Röhl, Schmid-Röhl, Oschmann, Frimmel, & Schwark, 2001). The euxinic depositional condition for the Dotternhausen black shale facies was determined by the existence of aryl isoprenoids (Figure 5), biomarkers for GSB (cf. Schwark & Frimmel, 2004), which implies relatively high aqueous hydrogen sulfide ( $\text{H}_2\text{S}$ ) concentration in the seawater. Such a seawater redox structure is further supported by the strong authigenic enrichment of redox-sensitive elements, that is, Mo, U, and V (Figure 5). For the Dotternhausen sedimentary profile, a gradual increase in aryl

isoprenoid concentration is exhibited in its lower part, followed by a decreasing trend in its upper part (Figure 5). The GSB, which are anoxygenic autotrophs, are able to oxidize  $\text{H}_2\text{S}$  to sulfate ( $\text{SO}_4^{2-}$ ) (e.g., Riccardi, Kump, Arthur, & D'Hondt, 2007). A bloom of GSB in the seawater will thus enhance the assimilative consumption of  $\text{H}_2\text{S}$  (Hurse, Kappler, & Keller, 2008), which can, to a certain extent, lower its concentration in the bottom anoxic/euxinic water mass, and thus deepen the seawater sulfidic oxygen minimum zone (chemocline). Alternatively, molecular oxygen generated by oxygenic photosynthesizers can also oxidize  $\text{H}_2\text{S}$  under high Eh conditions and thus change the depth of the seawater chemocline. However, this possibility is in conflict with the fact that GSB bloomed at c. 800 cm in the Dotternhausen profile (Figure 7), since GSB cannot thrive in oxic marine environments. In conclusion, if the chemocline is defined here as a relatively thick mid-depth water mass in which GSB progressively thrive (e.g., marked by the gradual increase in aryl isoprenoid concentration), the depositional environment of the Dotternhausen CIE sediments is considered to be characterized by a redox stratified seawater without a significant variation in the depth of the upper limit of this chemocline (Figure 8). In contrast, enhanced  $\text{H}_2\text{S}$  consumption in the bottom euxinic water mass during the height of GSB activity (maximum concentrations of aryl isoprenoid biomarkers) likely deepened the lower limit of the chemocline down to or near the water-sediment interface (Figure 8b). This favored higher fluxes

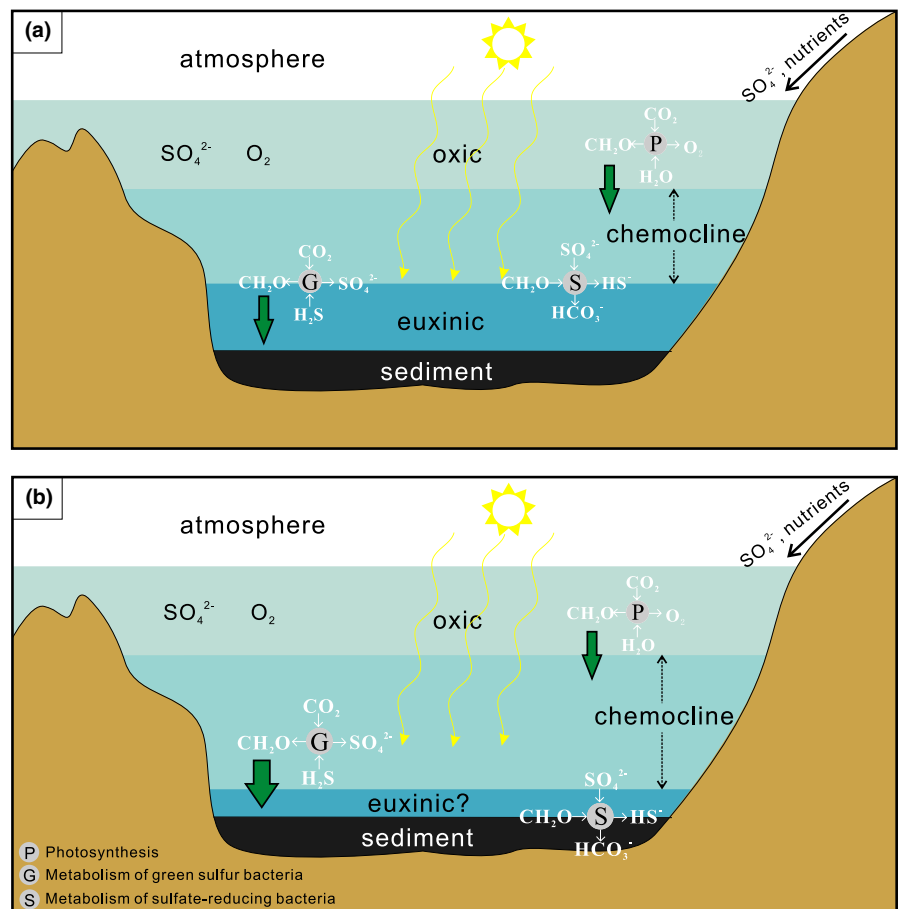


**FIGURE 8** Schematic representation of the Toarcian CIE northwestern Tethys seawater column during the gradual increase of GSB activity and associated  $\delta^{13}\text{C}_{\text{carb}} - \delta^{13}\text{C}_{\text{org}}$  decoupling. (a) Interval 2a: the initial stage of GSB bloom. (b) Interval 2b: the height of GSB bloom along with microbial sulfate reduction. The light, medium, and dark blue colors represent oxic, sulfidic oxygen minimum zone, and euxinic conditions, respectively, in the water column

of electron acceptors such as  $\text{SO}_4^{2-}$  and probably a small amount of manganese (Mn) oxyhydroxides (Figure 5 and Figure S1) to the sediment and thus fueled higher rate of dissimilatory reduction of  $\text{SO}_4^{2-}$  and Mn-oxyhydroxides. This caused an increase of organic carbon remineralization and promoted the formation of the diagenetic Unterer Stein lenticular carbonate bed.

### 5.3 | Evidence for second-order perturbations of the Toarcian carbon cycle

#### 5.3.1 | Decoupled $\delta^{13}\text{C}_{\text{carb}}$ - $\delta^{13}\text{C}_{\text{org}}$ superimposed on the Toarcian CIE in Dotternhausen, Germany

Carbon-cycle fluctuations in Earth's history such as the Mesozoic CIEs (Hesselbo et al., 2000; Kemp, Coe, Cohen, & Schwark, 2005; Kuypers, Pancost, & Damste, 1999) and Neoproterozoic Snowball Earth events (Och & Shields-Zhou, 2012; Sahoo et al., 2012) were commonly associated with changes in coeval  $\delta^{13}\text{C}_{\text{carb}}$  and  $\delta^{13}\text{C}_{\text{org}}$  records. Generally, a common approach used to distinguish whether a carbon cycle is global- or local scale is to evaluate the nature of the concurrently preserved  $\delta^{13}\text{C}_{\text{carb}}$  and  $\delta^{13}\text{C}_{\text{org}}$  signatures in sediments (Knoll, Hayes, Kaufman, Swett, & Lambert, 1986). Unpaired  $\delta^{13}\text{C}_{\text{carb}}$ - $\delta^{13}\text{C}_{\text{org}}$  is often suggested to have been impacted by second-order local-scale carbon-cycle perturbations (e.g., Jiang et al., 2012; Meyer et al., 2013); paired  $\delta^{13}\text{C}_{\text{carb}}$ - $\delta^{13}\text{C}_{\text{org}}$  is usually attributed to changes in the global carbon cycle (e.g., Ader et al., 2009; Li et al., 2018). It is widely accepted that the global injection of isotopically light carbon ( $\text{CH}_4$  and/or  $\text{CO}_2$ ) into the coeval atmosphere-ocean system during the early Toarcian led to widespread negative CIEs recorded in northwestern Tethys (e.g., Hesselbo et al., 2000; Hesselbo, Jenkyns, Duarte, & Oliveira, 2007; Svensen et al., 2007), eastern Tethys (Fu et al., 2016), southwestern Tethys (Ruebsam et al., 2020), south-eastern Tethys (Newton et al., 2011; Han, Hu, Kemp, & Li, 2018), northwestern Panthalassa (Izumi, Kemp, Itamiya, & Inui, 2018), and northeastern Panthalassa (Caruthers, Gröcke, & Smith, 2011). If the widespread Toarcian CIE was thus a global alteration of the carbon cycle, it is expected to be accompanied by a constant  $\Delta^{13}\text{C}_{\text{carb-org}}$  between DIC and DOC reservoirs. In this study, negative CIEs are observed in both  $\delta^{13}\text{C}_{\text{carb}}$  and  $\delta^{13}\text{C}_{\text{org}}$  records from the Dotternhausen section (Figure 7) of the northwestern Tethys (Figure 1). Pronounced  $\delta^{13}\text{C}_{\text{carb}}$ - $\delta^{13}\text{C}_{\text{org}}$  covariations have been shown in the lower (interval 1: 981–883 cm) and upper (interval 3: 757–613 cm) *falciferum* zone (Figure 9a,c) of the Toarcian CIE interval. Intervals 1 and 3 display relatively constant  $\Delta^{13}\text{C}_{\text{carb-org}}$  values around 27‰ and 28‰, respectively (Figures 7 and 10a), which most likely reflect global-scale carbon-cycle perturbations during the Toarcian. However, a prominent two-step  $\delta^{13}\text{C}_{\text{carb}}$ - $\delta^{13}\text{C}_{\text{org}}$  decoupling signature, along with two distinct magnitudes of decreased  $\Delta^{13}\text{C}_{\text{carb-org}}$  values, is observed around the climax of the CIE (interval 2a and 2b; Figures 7 and 10a), which points to a local-scale disturbance of the carbon cycle. The first step in interval 2a is of smaller magnitude compared to the much larger second step in interval 2b (Figures 7 and 10a).

#### 5.3.2 | Possible mechanism(s) for the local-scale $\delta^{13}\text{C}_{\text{carb}}$ - $\delta^{13}\text{C}_{\text{org}}$ decoupling

##### Interval 2a

The negative excursion in  $\Delta^{13}\text{C}_{\text{carb-org}}$  is more influenced by the variation in the  $\delta^{13}\text{C}_{\text{carb}}$  than  $\delta^{13}\text{C}_{\text{org}}$  values (Figure 7). However, carbonates in the black shales of interval 2a represent a combination of biogenic calcites related to calcareous phytoplankton (Frimmel, Oschmann, & Schwark, 2004) and disseminated authigenic grains. A rough estimate of contribution from organic matter remineralization ( $\text{C}_{\text{org}}$ ) and seawater inorganic carbon ( $\text{C}_{\text{sw}}$ ) in carbonate can be obtained with the following equation (cf. Heimann et al., 2010; Konhauser et al., 2017):

$$[\text{DIC}]_{\text{total}} \times \delta^{13}\text{C}_{\text{total}} = [\text{DIC}]_{\text{org}} \times \delta^{13}\text{C}_{\text{org}} + [\text{DIC}]_{\text{sw}} \times \delta^{13}\text{C}_{\text{sw}}$$

where the  $[\text{DIC}]_{\text{total}}$ ,  $[\text{DIC}]_{\text{org}}$ , and  $[\text{DIC}]_{\text{sw}}$  denote total inorganic carbon, inorganic carbon derived from remineralized organic matter, and inorganic carbon from seawater;  $\delta^{13}\text{C}_{\text{total}}$  and  $\delta^{13}\text{C}_{\text{sw}}$  denote the  $\delta^{13}\text{C}$  of total carbonate ( $\delta^{13}\text{C}_{\text{carb}}$ ) and seawater. Assuming that the  $\delta^{13}\text{C}$  values of Phanerozoic  $[\text{DIC}]_{\text{sw}}$  is near to zero (Shields & Veizer, 2002 and references therein),  $[\text{DIC}]_{\text{org}}$  (equals to  $([\text{DIC}]_{\text{total}} \times \delta^{13}\text{C}_{\text{total}}) / \delta^{13}\text{C}_{\text{org}}$ ) varies between 13% and 28%  $[\text{DIC}]_{\text{total}}$  (average of 20%) (Table 2), while  $[\text{DIC}]_{\text{sw}}$  has an average of 80%. This estimate can be translated by the  $\delta^{13}\text{C}_{\text{carb}}$  versus  $\delta^{18}\text{O}$  cross-plots (Figure 10b; Konhauser et al., 2017; Ossa Ossa et al., 2018). The samples of the interval 2a have  $\delta^{13}\text{C}_{\text{carb}}$  values between  $-8.8$  and  $-4.2$ ‰ and almost all of them plot above the line of  $\text{C}_{\text{org}} : \text{C}_{\text{sw}} = 1:1$  (Figure 10b). This implies that carbon components of these carbonates are contributed by  $\sim 80\%$  of DIC and only  $\sim 20\%$  of remineralized organic carbon (Figure 10b). The remineralization of organic matter occurs through anaerobic or microaerophilic microbial processes that require electron acceptors (e.g., Heimann et al., 2010; Konhauser et al., 2017 and references therein), which here are sulfate and possibly Mn-oxyhydroxides (see Section 5.2). These processes produce carbonates with lighter  $\delta^{13}\text{C}_{\text{carb}}$  values compared to the ambient DIC composition.

It can be noticed that the shift toward negative  $\delta^{13}\text{C}_{\text{carb}}$  values in interval 2a is accompanied by a very minor shift of  $\delta^{13}\text{C}_{\text{org}}$  toward heavier values (Figure 7). The metabolisms of anoxygenic photoautotrophs (GSB) yield  $^{13}\text{C}$ -enriched biomass through primary productivity (Takahashi, Kaiho, Oba, & Kakegawa, 2010; van Breugel, Baas, Schouten, Mattioli, & Sinninghe Damsté, 2006) and can explain the small increase in  $\delta^{13}\text{C}_{\text{org}}$  values observed in interval 2a. However, since this  $\delta^{13}\text{C}_{\text{org}}$  increase is minimal, it does not have a major impact on the overall  $\Delta^{13}\text{C}_{\text{carb-org}}$  negative excursion—though this interval represents the early stage of the GSB bloom. In view of this, carbonates in the interval 2a precipitated in equilibrium with seawater isotope composition, but were further aided by a small contribution of isotopically lighter carbon generated through microbial-induced organic carbon remineralization (Figure 8a). This small contribution of light carbon isotopes likely explains the smaller magnitude of the  $\Delta^{13}\text{C}_{\text{carb-org}}$  negative excursion recorded in this interval.

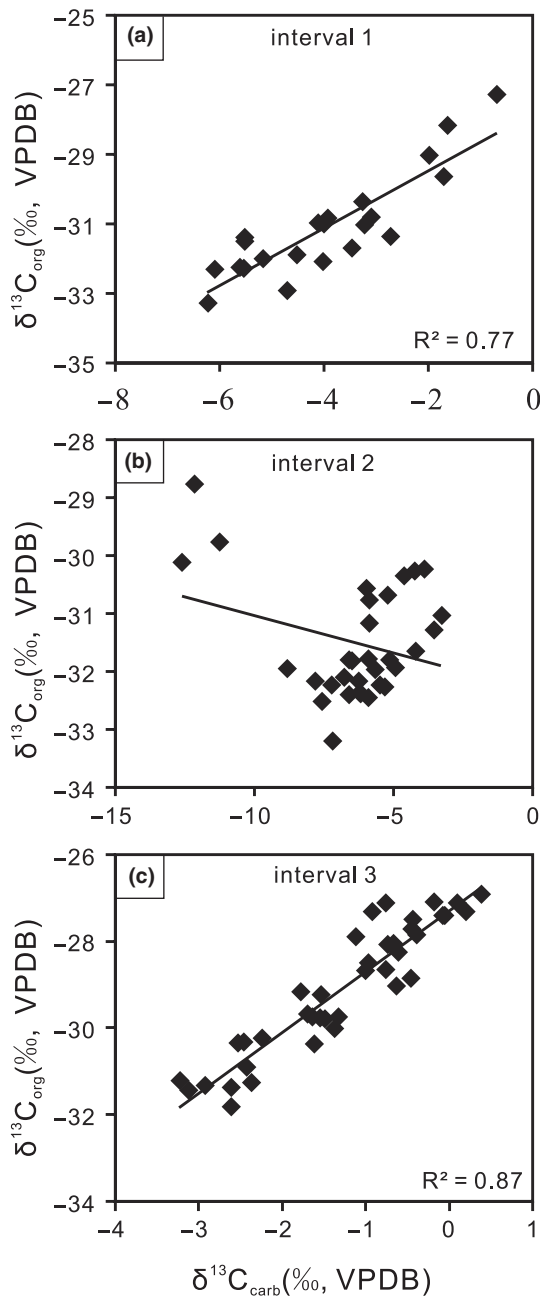


**FIGURE 9** Crossplots of  $\delta^{13}\text{C}_{\text{carb}}-\delta^{13}\text{C}_{\text{org}}$  in different intervals of the Dotternhausen carbon isotopic profiles

#### Interval 2b

The negative  $\Delta^{13}\text{C}_{\text{carb-orig}}$  excursion in this interval is accompanied by a shift to heavier  $\delta^{13}\text{C}_{\text{org}}$  and lighter  $\delta^{13}\text{C}_{\text{carb}}$  values (Figure 7). Assuming that diagenesis of organic-rich sediments is widely described to have a minimal effect on  $\delta^{13}\text{C}_{\text{org}}$  values (e.g., Jiang et al., 2012; Watanabe et al., 1997), it cannot thus explain the positive shift in  $\delta^{13}\text{C}_{\text{org}}$  values recorded in interval 2b (see Section 5.1). This  $\delta^{13}\text{C}_{\text{org}}$  record rather reflects a pristine isotope signal imparted by the dominant productive marine biota. As stated above (see interval 2a), the biomass produced by GSB is  $^{13}\text{C}$ -enriched. Across interval 2b the height of GSB activity is obviously indicated by the maximum

concentration of aryl isoprenoid biomarkers, which generated more isotopically heavy biomass and the associated  $\delta^{13}\text{C}_{\text{org}}$  positive excursion (Figure 7). The  $\delta^{13}\text{C}_{\text{carb}}-\delta^{13}\text{C}_{\text{org}}$  decoupling in interval 2b can thus partly be explained by the climax of GSB metabolism.

Importantly, interval 2b includes changes in lithofacies from carbonate-bearing laminated black shales in its lowermost part to the diagenetic Unterer Stein carbonate bed upward and then back to carbonate-bearing laminated black shales (Figure 7). Therefore, the light carbon isotope composition of the Unterer Stein may be dominantly attributed to diagenetic carbonate precipitation through microbial sulfate reduction (MSR) with a minor contribution from dissimilatory Mn-oxyhydroxides reduction (see Section 5.2). Such diagenetic processes produce carbonates with light  $\delta^{13}\text{C}_{\text{carb}}$  values, which may enhance the negative  $\Delta^{13}\text{C}_{\text{carb-orig}}$  excursion in this interval (cf. Heimann et al., 2010; Konhauser et al., 2017). However, the  $\delta^{13}\text{C}_{\text{carb}}$  versus  $\delta^{18}\text{O}$  diagram indicates that the limestone bed samples fall between  $\text{C}_{\text{org}}:\text{C}_{\text{sw}} = 1:1$  and  $\text{C}_{\text{org}}:\text{C}_{\text{sw}} = 1:2$  lines (Figure 10b), and the calculated  $[\text{DIC}]_{\text{org}}$  values vary between 38% and 42%  $[\text{DIC}]_{\text{total}}$  (41% on average). This implies relatively greater amounts of carbon components derived from organic matter remineralization during diagenesis, compared to those in interval 2a—though the  $\text{DIC}_{\text{sw}}$  was still a major contributor in this carbonate bed. In contrast, samples from the carbonate-bearing laminated black shales (lowermost and upper parts of interval 2b) are exclusively distributed above the  $\text{C}_{\text{org}}:\text{C}_{\text{sw}} = 1:3$  line (Figure 10b) with the calculated average  $[\text{DIC}]_{\text{org}}$  value of 17%, demonstrating that their carbonate carbon components were mainly sourced from  $\text{DIC}_{\text{sw}}$ . It follows that the sediment pore waters or diagenetic environment in which the lenticular Unterer Stein carbonate bed precipitated was still in equilibrium with seawater. However, carbonate grains in the laminated black shale could have precipitated either in the water column or in sediments. Therefore, the  $\delta^{13}\text{C}_{\text{org}}-\delta^{13}\text{C}_{\text{carb}}$  decoupling in interval 2b was largely caused by a GSB bloom and further exaggerated by the remineralization of organic material by MSR through authigenic carbonate precipitation (see Section 5.2; Figure 8b).

In summary, the coeval decreases in  $\delta^{13}\text{C}_{\text{carb}}$  and increases in  $\delta^{13}\text{C}_{\text{org}}$  values, which contributed to the two-step  $\Delta^{13}\text{C}_{\text{carb-orig}}$  decoupling in interval 2, reflect a combined effect of enhanced activity of GSB and sulfate-reducing bacteria (SRB) (Figure 8). The GSB bloom caused high  $\text{H}_2\text{S}$  consumption in the euxinic bottom water and likely expanded the chemocline near to the water-sediment interface. This allowed higher sulfate flux to the anoxic sediment pore waters and ultimately caused carbonate precipitation aided by higher rates of SRB-induced organic carbon remineralization. In contrast, the following coeval increase in  $\delta^{13}\text{C}_{\text{carb}}$  and decrease in  $\delta^{13}\text{C}_{\text{org}}$  values, which ended this two-step  $\Delta^{13}\text{C}_{\text{carb-orig}}$  decoupling in the upper part of interval 2b, were mainly caused by a decline of GSB activity as a consequence of exhausted  $\text{H}_2\text{S}$  availability in the water column. However, interval 2b represents the peak of the GSB bloom and explains the more pronounced  $\Delta^{13}\text{C}_{\text{carb-orig}}$  decoupling in this interval compared to the lower 2a. Interestingly, this GSB bloom in interval 2 might have consumed enough  $\text{H}_2\text{S}$  in the Toarcian OAE water column to re-establish environmental conditions favorable for an increased expansion of aerobic metabolisms,

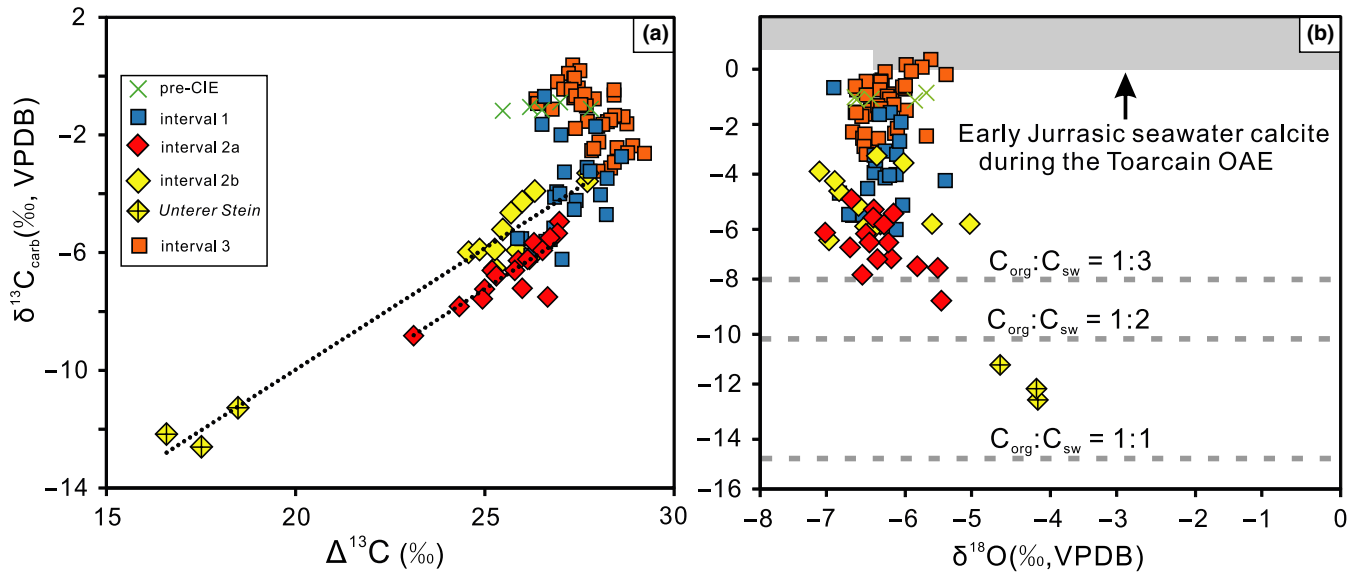


**FIGURE 10** Crossplots of  $\delta^{13}\text{C}_{\text{carb}}$  vs  $\Delta^{13}\text{C}$  (a) and  $\delta^{13}\text{C}_{\text{carb}}$  vs  $\delta^{18}\text{O}$  (b) for different sedimentary intervals in the Dotternhausen. (a) The interval 2a (black shales) and 2b (Unterer Stein and black shales) show strong correlations between  $\delta^{13}\text{C}_{\text{carb}}$  and  $\Delta^{13}\text{C}$ . (b) An model showing the carbonate carbon contribution between organic matter oxidation ( $C_{\text{org}}$ ) and seawater inorganic carbon ( $C_{\text{sw}}$ ) (cf. Heimann et al., 2010; Konhauser et al., 2017). The isotope composition of early Jurassic seawater calcites during Toarcian OAE were estimated from the belemnites ( $\delta^{13}\text{C}_{\text{bel}}$ :  $\sim 0$  to  $+2\text{‰}$  and  $\delta^{18}\text{O}_{\text{bel}}$ :  $\sim -6$  to  $0\text{‰}$ ; Ullmann, Thibault, Ruhl, Hesselbo, & Korte, 2014) and platform limestone ( $\delta^{13}\text{C}_{\text{limestone}}$ :  $\sim +1$  to  $+2\text{‰}$  and  $\delta^{18}\text{O}_{\text{limestone}}$ :  $\sim -8$  to  $-5\text{‰}$ ; Han, Hu, Kemp, & Li, 2018)

that is, oxygenic photosynthesis, and ultimately trigger the progressive recovery to the end of the Toarcian CIE observed in the overlying interval 3 (Figure 7).

### 5.3.3 | Implication for ecosystem structure on local-scale carbon-cycle perturbation

A previous study has shown that co-varying  $\delta^{13}\text{C}_{\text{carb}}$  and  $\delta^{13}\text{C}_{\text{org}}$  imply that organic carbon in marine sediments is mainly derived from primary (photosynthetic) production without substantial post-depositional alteration (cf. Jiang et al., 2012). Here, it is shown that an abrupt carbon-cycle perturbation by intense metabolisms of GSB has the capacity of decoupling the primary carbon isotopic signals. In Earth's history, the dramatic rise in GSB activity is not only limited to Toarcian OAE epicontinental seas (Pancost et al., 2004; Röhl, Schmid-Röhl, Oschmann, Frimmel, & Schwark, 2001; Sælen, Tyson, Telnæs, & Talbot, 2000; Schwark & Frimmel, 2004; van Breugel, Baas, Schouten, Mattioli, & Sinninghe Damsté, 2006; Xu et al., 2018), but also significant in a number of ancient marine realms during the end-Ordovician, end-Devonian, end-Permian and end-Triassic mass-extinction events, which were, at least in part, forced by an increase in  $\text{H}_2\text{S}$  in the seawater (e.g., Joachimski et al., 2001; Riccardi, Kump, Arthur, & D'Hondt, 2007; Richoz et al., 2012). Decoupled  $\delta^{13}\text{C}_{\text{carb}}-\delta^{13}\text{C}_{\text{org}}$  signals across these mass extinctions broadly coincide with enhanced GSB activities (van de Schootbrugge & Gollner, 2013, and references therein), which

implies the potential role of GSB in perturbing coeval carbon cycling. Thus, to investigate the possible mechanisms for decoupling  $\delta^{13}\text{C}_{\text{carb}}-\delta^{13}\text{C}_{\text{org}}$  in sedimentary rocks, carbon-cycle turnover arising from a sharp proliferation of GSB may play a major role and should not be neglected.

### 5.4 | Tethys-wide but locally variable second-order perturbations of the Toarcian carbon cycle

Theoretically, coupled  $\delta^{13}\text{C}_{\text{carb}}-\delta^{13}\text{C}_{\text{org}}$  signatures are expected in all existing Toarcian OAE sedimentary sections due to the global scale of this event (described in Section 5.3.1). Opposed to this expectation, however, decoupled  $\delta^{13}\text{C}_{\text{carb}}-\delta^{13}\text{C}_{\text{org}}$  signals (yellow areas in Figure 11a and yellow squares in Figure 11b) are also found in other Toarcian OAE profiles, such as Bilong Co (eastern Tethys: Fu et al., 2016), Sancerre (northwestern Tethys: Hermoso et al., 2012), and Nianduo (southeastern Tethys: Han, Hu, Kemp, & Li, 2018), apart from the Dotternhausen one. This indicates that second-order carbon-cycle perturbations pervasively existed in anoxic/euxinic restricted basins and unrestricted marginal seas throughout Tethyan margin across the Toarcian OAE. Both, the Bilong Co and Sancerre sections, show coupled  $\delta^{13}\text{C}_{\text{carb}}-\delta^{13}\text{C}_{\text{org}}$  below and above the decoupling interval (blue and orange areas in Figure 11a; blue and orange squares in Figure 11b), similar to the Dotternhausen profile. By contrast, the Nianduo CIE profile does not exhibit such coupled  $\delta^{13}\text{C}_{\text{carb}}-\delta^{13}\text{C}_{\text{org}}$  intervals (Figure 11c),

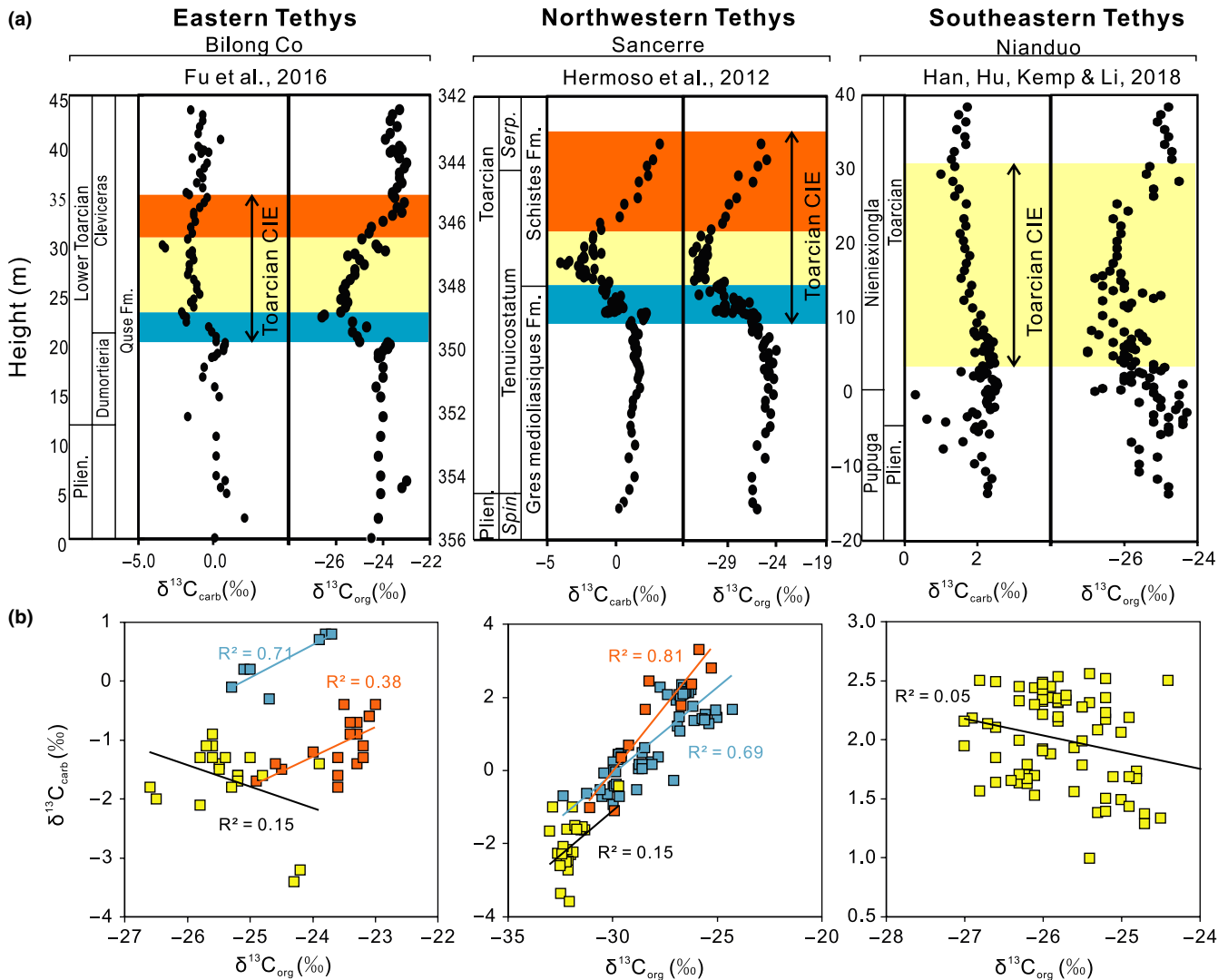


**FIGURE 11**  $\delta^{13}\text{C}_{\text{carb}}-\delta^{13}\text{C}_{\text{org}}$  decoupling signals (yellow areas in panel (a) and yellow squares in panel (b)) from geographically distinct localities (Bilong Co in eastern Tethys, Fu et al., 2016; Sancerre in northwestern Tethys, Hermoso et al., 2012; Nianduo in southeastern Tethys, Han et al., 2018) are identified across Toarcian CIE shown in panel A. Blue and orange colors in both panel A and B standing for the observed coupled  $\delta^{13}\text{C}_{\text{carb}}-\delta^{13}\text{C}_{\text{org}}$  signals across Toarcian CIE are comparable to the marked interval 1 and 3 in the studied Dotternhausen section. Fm., formation; Plien., Pliensbachian; Serp., Serpentinum; Spin., Spinatum

which for the southeastern Tethys implies persistent local carbon-cycling disturbances throughout the entire Toarcian OAE. It should be noted that the  $\delta^{13}\text{C}_{\text{carb}}$  profiles of the various Toarcian sedimentary sections throughout the entire Toarcian CIE are strikingly different from one another, and so are the  $\delta^{13}\text{C}_{\text{org}}$  profiles, respectively (Figures 7 and 11). Interestingly,  $\delta^{13}\text{C}_{\text{org}}$  and  $\delta^{13}\text{C}_{\text{carb}}$  throughout the decoupled sections of the various profiles also behave very differently, even when deposited in similar regions of the Tethys Ocean. For example,  $\delta^{13}\text{C}_{\text{org}}$  in the decoupled part of the Sancerre section (NW-Tethys) is characterized by relatively constant values, whereas  $\delta^{13}\text{C}_{\text{carb}}$  values strongly decrease and then increase again. In the decoupled part of the Dotternhausen section (NW-Tethys)  $\delta^{13}\text{C}_{\text{org}}$  values are increasing, while the corresponding  $\delta^{13}\text{C}_{\text{carb}}$  values are decreasing (Figures 7 and 11). This

difference in the C isotope stratigraphies of the two sections may be tied to the hydrographically restricted conditions (McArthur, 2019; McArthur et al., 2008; Ruvalcaba Baroni et al., 2018) that prevented water mass exchange between the two basins. However, further detailed work beyond the scope of this study is needed to understand the  $\delta^{13}\text{C}_{\text{carb}}-\delta^{13}\text{C}_{\text{org}}$  decoupling patterns observed in the various Toarcian OAE sections.

## 6 | CONCLUSION

The black shale facies in the Dotternhausen section was deposited in a redox stratified marine environment and was not significantly impacted by terrestrial-sourced organic carbon, thermal maturity,



and hydrothermal fluids. Two prominent decoupled  $\delta^{13}\text{C}_{\text{carb}}$ - $\delta^{13}\text{C}_{\text{org}}$  signals superimpose the Toarcian CIE in the Dotternhausen section, southwest Germany. The stratigraphically first  $\delta^{13}\text{C}_{\text{carb}}$ - $\delta^{13}\text{C}_{\text{org}}$  decoupling (shown in black shales in interval 2a) was of a small magnitude and most likely caused by a carbon-cycle disturbance from the onset of GSB metabolic activity. The second and in magnitude much larger decoupling in interval 2b resulted from a GSB bloom, but was further exaggerated by early diagenetic effects. Thereby, dissimilatory respiration of SRB led to the formation of  $^{12}\text{C}$ -enriched authigenic calcites within the sediment throughout organic matter remineralization. This process amplified the  $\delta^{13}\text{C}_{\text{carb}}$ - $\delta^{13}\text{C}_{\text{org}}$  decoupling between the diagenetic carbonate (Unterer Stein) and the remaining organic matter. The  $\delta^{13}\text{C}_{\text{carb}}$  and  $\delta^{13}\text{C}_{\text{org}}$  profiles from geographically distinct Toarcian OAE localities (e.g., Bilong Co, Nianduo, and Sancerre) in the Tethys region show strong variability in their  $\delta^{13}\text{C}_{\text{carb}}$ - $\delta^{13}\text{C}_{\text{org}}$  decoupling signals, which indicates the substantial impact of local carbon-cycle perturbations on the global carbon cycle during the Toarcian CIE.

#### ACKNOWLEDGMENTS

We are grateful for the help and technical support from Elmar Reitter and Bernd Steinhilber in the laboratory. We thank Holcim GmbH Dotternhausen for access to their quarry and for providing drillcore materials for this study. Y.W. thanks the China Scholarship Council (CSC) for his financial support. We are grateful to the two anonymous reviewers and to the Editor N. Planavsky for their comments and suggestions that highly improved the original manuscript. We would also like to thank the Editor K. Konhauser for handling this manuscript. Open access funding enabled and organized by Projekt DEAL.

#### CONFLICT OF INTEREST

The authors declare no conflict of interest and no compelling financial interests.

#### ORCID

Yunfeng Wang  <https://orcid.org/0000-0001-6818-1061>

#### REFERENCES

- Ader, M., Macouin, M., Trindade, R. I. F., Hadrien, M., Yang, Z. Y., Sun, Z. M., & Besse, J. (2009). A multilayered water column in the Ediacaran Yangtze platform? Insights from carbonate and organic matter paired  $\delta^{13}\text{C}$ . *Earth and Planetary Science Letters*, 288, 213–227. <https://doi.org/10.1016/j.epsl.2009.09.024>
- Albut, G., Babechuk, M. G., Kleinhans, I. C., Bengler, M., Beukes, N. J., Steinhilber, B., ... Schoenberg, R. (2018). Modern rather than Mesoarchaeon oxidative weathering responsible for the heavy stable Cr isotopic signatures of the 2.95 Ga old Ijzermijn iron formation (South Africa). *Geochimica et Cosmochimica Acta*, 228, 157–189. <https://doi.org/10.1016/j.gca.2018.02.034>
- Aries, S., Valladon, M., Polvé, M., & Dupré, B. (2007). A routine method for oxide and hydroxide interference corrections in ICP-MS chemical analysis of environmental and geological samples. *Geostandards Newsletter*, 24, 19–31. <https://doi.org/10.1111/j.1751-908X.2000.tb00583.x>
- Babechuk, M. G., Widdowson, M., Murphy, M., & Kamber, B. S. (2015). A combined Y/Ho, high field strength element (HFSE) and Nd isotope perspective on basal weathering, Deccan Traps, India. *Chemical Geology*, 396, 25–41. <https://doi.org/10.1016/j.chemgeo.2014.12.017>
- Baudin, F., Herbin, J.-P., & Vandenbroucke, M. (1990). Mapping and geochemical characterization of the Toarcian organic matter in the Mediterranean Tethys and Middle East. *Advances in Organic Geochemistry*, 16, 677–687. [https://doi.org/10.1016/0146-6380\(90\)90109-D](https://doi.org/10.1016/0146-6380(90)90109-D)
- Bjerrum, C. J., Surlyk, F., Callomon, J. H., & Slingerland, R. L. (2001). Numerical paleoceanographic study of the Early Jurassic transcontinental Laurasian Seaway. *Paleoceanography*, 16, 390–404. <https://doi.org/10.1029/2000pa000512>
- Bour, I., Mattioli, E., & Pittet, B. (2007). Nannofacies analysis as a tool to reconstruct paleoenvironmental changes during the Early Toarcian anoxic event. *Palaeogeography, Palaeoclimatology, Palaeoecology*, 249, 58–79. <https://doi.org/10.1016/j.palaeo.2007.01.013>
- Caruthers, A. H., Gröcke, D. R., & Smith, P. L. (2011). The significance of an Early Jurassic (Toarcian) carbon-isotope excursion in Haida Gwaii (Queen Charlotte Islands), British Columbia, Canada. *Earth and Planetary Science Letters*, 307, 19–26. <https://doi.org/10.1016/j.epsl.2011.04.013>
- Cohen, A. S., Coe, A. L., Harding, S. M., & Schwark, L. (2004). Osmium isotope evidence for the regulation of atmospheric  $\text{CO}_2$  by continental weathering. *Geology*, 32, 157–160. <https://doi.org/10.1130/g20158.1>
- Danise, S., Twitchett, R. J., & Little, C. T. S. (2015). Environmental controls on Jurassic marine ecosystems during global warming. *Geology*, 43, 263–266. <https://doi.org/10.1130/g36390.1>
- Dembicki, H. Jr (2009). Three common source rock evaluation errors made by geologists during prospect or play appraisals. *AAPG bulletin*, 93, 341–356. <https://doi.org/10.1306/10230808076>
- Guillaume, D., & Yannick, D. (2012). Modeling evidences for global warming, Arctic seawater freshening, and sluggish oceanic circulation during the Early Toarcian anoxic event. *Paleoceanography and Paleoclimatology*, 27, PA2211. <https://doi.org/10.1029/2012PA002283>
- de Kock, M. O., Beukes, N. J., Adeniyi, E. O., Cole, D., Gotz, A. E., Geel, C., & Ossa Ossa, F. (2017). Deflating the shale gas potential of South Africa's Main Karoo basin. *South African Journal of Science*, 113, 1–12. <https://doi.org/10.17159/sajs.2017/20160331>
- Fantasia, A., Föllmi, K. B., Adatte, T., Spangenberg, J. E., & Montero-Serrano, J.-C. (2018). The early toarcian oceanic anoxic event: Paleoenvironmental and paleoclimatic change across the Alpine Tethys (Switzerland). *Global and Planetary Change*, 162, 53–68. <https://doi.org/10.1016/j.gloplacha.2018.01.008>
- Francois, R. (1988). A study on the regulation of the concentrations of some trace metals (Rb, Sr, Zn, Pb, Cu, V, Cr, Ni, Mn and Mo) in Saanich Inlet sediments, British Columbia, Canada. *Marine Geology*, 83, 285–308. [https://doi.org/10.1016/0025-3227\(88\)90063-1](https://doi.org/10.1016/0025-3227(88)90063-1)
- French, K. L., Sepulveda, J., Trabucho-Alexandre, J., Gröcke, D. R., & Summons, R. E. (2014). Organic geochemistry of the early Toarcian oceanic anoxic event in Hawsker Bottoms, Yorkshire, England. *Earth and Planetary Science Letters*, 390, 116–127. <https://doi.org/10.1016/j.epsl.2013.12.033>
- Frimmel, A. (2003). *Hochauflösende Untersuchungen von Biomarkern an epikontinentalen Schwarzschiefern des Unteren Toarciums (Posidonienschiefer, Lias e) von SW-Deutschland (in German with English abstract)*. Retrieved from <https://publikationen.uni-tuebingen.de/xmlui/handle/10900/48450>
- Frimmel, A., Oschmann, W., & Schwark, L. (2004). Chemostratigraphy of the Posidonia Black Shale, SW Germany I. Influence of sea-level variation on organic facies evolution. *Chemical Geology*, 206, 199–230. <https://doi.org/10.1016/j.chemgeo.2003.12.007>
- Fu, X., Wang, J., Feng, X., Wang, D., Chen, W., Song, C., & Zeng, S. (2016). Early Jurassic carbon-isotope excursion in the Bilong Co Basin (Tibet), the eastern Tethys: Implications for the Toarcian Oceanic anoxic

- event. *Chemical Geology*, 442, 62–72. <https://doi.org/10.1016/j.chemgeo.2016.09.007>
- Govindaraju, K., & Roelandts, I. (1989). 1988 compilation report on trace elements in six ANRT rock reference samples: diorite DR-N, serpentine UB-N, bauxite BX-N, disthene DT-N, granite GS-N and potash feldspar FK-N. *Geostandards Newsletter*, 13, 5–67. <https://doi.org/10.1111/j.1751-908X.1989.tb00465.x>
- Han, Z., Hu, X., Kemp, D. B., & Li, J. (2018). Carbonate-platform response to the Toarcian Oceanic Anoxic Event in the southern hemisphere: Implications for climatic change and biotic platform demise. *Earth and Planetary Science Letters*, 489, 59–71. <https://doi.org/10.1016/j.epsl.2018.02.017>
- Heimann, A., Johnson, C. M., Beard, B. L., Valley, J. W., Roden, E. E., Spicuzza, M. J., & Beukes, N. J. (2010). Fe, C, and O isotope compositions of banded iron formation carbonates demonstrate a major role for dissimilatory iron reduction in ~2.5 Ga marine environments. *Earth and Planetary Science Letters*, 294, 8–18. <https://doi.org/10.1016/j.epsl.2018.07.044>
- Hermoso, M., Minoletti, F., & Pellenard, P. (2013). Black shale deposition during Toarcian super-greenhouse driven by sea level. *Climate of the Past*, 9, 2703–2712. <https://doi.org/10.5194/cp-9-2703-2013>
- Hermoso, M., Minoletti, F., Rickaby, R. E., Hesselbo, S. P., Baudin, F., & Jenkyns, H. C. (2012). Dynamics of a stepped carbon-isotope excursion: Ultra high-resolution study of Early Toarcian environmental change. *Earth and Planetary Science Letters*, 319, 45–54. <https://doi.org/10.1016/j.epsl.2011.12.021>
- Hesselbo, S. P., Gröcke, D. R., Jenkyns, H. C., Bjerrum, C. J., Farrimond, P., Bell, H. S. M., & Green, O. W. (2000). Massive dissociation of gas hydrate during a Jurassic oceanic anoxic event. *Nature*, 406, 392–395. <https://doi.org/10.1038/35019044>
- Hesselbo, S. P., Jenkyns, H. C., Duarte, L. V., & Oliveira, L. C. V. (2007). Carbon-isotope record of the Early Jurassic (Toarcian) Oceanic Anoxic Event from fossil wood and marine carbonate (Lusitanian Basin, Portugal). *Earth and Planetary Science Letters*, 253, 455–470. <https://doi.org/10.1016/j.epsl.2006.11.009>
- Hinrichs, K. U. (2002). Microbial fixation of methane carbon at 2.7 Ga: Was an anaerobic mechanism possible? *Geochemistry, Geophysics, Geosystems*, 3, 1–10. <https://doi.org/10.1029/2001GC000286>
- Hurse, T. J., Kappler, U., & Keller, J. (2008). *Using anoxygenic photosynthetic bacteria for the removal of sulfide from wastewater*. [https://doi.org/10.1007/978-1-4020-6863-8\\_22](https://doi.org/10.1007/978-1-4020-6863-8_22)
- Izumi, K., Kemp, D. B., Itamiya, S., & Inui, M. (2018). Sedimentary evidence for enhanced hydrological cycling in response to rapid carbon release during the early Toarcian oceanic anoxic event. *Earth and Planetary Science Letters*, 481, 162–170. <https://doi.org/10.1016/j.epsl.2017.10.030>
- Jenkyns, H. C. (1988). The early Toarcian (Jurassic) anoxic event; stratigraphic, sedimentary and geochemical evidence. *American Journal of Science*, 288, 101–151. <https://doi.org/10.2475/ajs.288.2.101>
- Jenkyns, H. C. (2010). Geochemistry of oceanic anoxic events. *Geochemistry, Geophysics, Geosystems*, 11(3). <https://doi.org/10.1029/2009gc002788>
- Jenkyns, H. C., Jones, C. E., Gröcke, D. R., Hesselbo, S. P., & Parkinson, D. N. (2002). Chemostratigraphy of the Jurassic System: Applications, limitations and implications for palaeoceanography. *Journal of the Geological Society*, 159, 351–378. <https://doi.org/10.1144/0016-764901-130>
- Jiang, G., Wang, X., Shi, X., Xiao, S., Zhang, S., & Dong, J. (2012). The origin of decoupled carbonate and organic carbon isotope signatures in the early Cambrian (ca. 542–520 Ma) Yangtze platform. *Earth and Planetary Science Letters*, 317–318, 96–110. <https://doi.org/10.1016/j.epsl.2011.11.018>
- Joachimski, M. M., Ostertag-Henning, C., Pancost, R. D., Strauss, H., Freeman, K. H., Littke, R., ... Racki, G. (2001). Water column anoxia, enhanced productivity and concomitant changes in  $\delta^{13}\text{C}$  and  $\delta^{34}\text{S}$  across the Frasnian-Famennian boundary (Kowala–Holy Cross Mountains/Poland). *Chemical Geology*, 175, 109–131. [https://doi.org/10.1016/S0009-2541\(00\)00365-X](https://doi.org/10.1016/S0009-2541(00)00365-X)
- Kamber, B. S., Webb, G. E., & Gallagher, M. (2014). The rare earth element signal in Archaean microbial carbonate: information on ocean redox and biogenicity. *Journal of the Geological Society*, 171, 745–763. <https://doi.org/10.1144/jgs2013-110>
- Kemp, D. B., Coe, A. L., Cohen, A. S., & Schwark, L. (2005). Astronomical pacing of methane release in the Early Jurassic period. *Nature*, 437, 396–399. <https://doi.org/10.1038/nature04037>
- Konhauser, K. O., Planavsky, N. J., Hardisty, D. S., Robbins, L. J., Warchola, T. J., Haugaard, R., ... Lyons, T. W. (2017). Iron formations: A global record of Neoproterozoic to Palaeoproterozoic environmental history. *Earth-Science Reviews*, 172, 140–177. <https://doi.org/10.1016/j.earscirev.2017.06.012>
- Knoll, A. H., Hayes, J. M., Kaufman, A. J., Swett, K., & Lambert, I. B. (1986). Secular variation in carbon isotope ratios from Upper Proterozoic successions of Svalbard and East Greenland. *Nature*, 321, 832–838. <https://doi.org/10.1038/321832a0>
- Kuhn, O., & Etter, W. (1994). Der Posidonienschiefer der Nordschweiz: Lithostratigraphie, Biostratigraphie und Fazies. *Eclogae Geologicae Helveticae*, 87, 113–138.
- Kuypers, M. M., Pancost, R. D., & Damste, J. S. S. (1999). A large and abrupt fall in atmospheric  $\text{CO}_2$  concentration during Cretaceous times. *Nature*, 399, 342–345. <https://doi.org/10.1038/20659>
- Li, D., Zhang, X., Hu, D., Chen, X., Huang, W., Zhang, X., ... Shen, Y. (2018). Evidence of a large  $\delta^{13}\text{C}_{\text{carb}}$  and  $\delta^{13}\text{C}_{\text{org}}$  depth gradient for deep-water anoxia during the late Cambrian SPICE event. *Geology*, 47, 115–118. <https://doi.org/10.1130/G45709.1>
- Little, C. T., & Benton, M. J. (1995). Early Jurassic mass extinction: A global long-term event. *Geology*, 23, 495–498. [https://doi.org/10.1130/0091-7613\(1995\)023<0495:EJMEAG>2.3.CO;2](https://doi.org/10.1130/0091-7613(1995)023<0495:EJMEAG>2.3.CO;2)
- Maloof, A. C., Porter, S. M., Moore, J. L., Dudás, F. Ö., Bowring, S. A., Higgins, J. A., ... Eddy, M. P. (2010). The earliest Cambrian record of animals and ocean geochemical change. *Geological Society of America Bulletin*, 122, 1731–1774. <https://doi.org/10.1130/b30346.1>
- Mattioli, E., Pittet, B., Suan, G., & Mailliot, S. (2008). Calcareous nanoplankton changes across the early Toarcian oceanic anoxic event in the western Tethys. *Paleoceanography*, 23, PA3208. <https://doi.org/10.1029/2007PA001435>
- McArthur, J. M. (2019). Early Toarcian black shales: A response to an oceanic anoxic event or anoxia in marginal basins? *Chemical Geology*, 522, 71–83. <https://doi.org/10.1016/j.chemgeo.2019.05.028>
- McArthur, J. M., Algeo, T. J., van de Schootbrugge, B., Li, Q., & Howarth, R. J. (2008). Basinal restriction, black shales, Re-Os dating, and the Early Toarcian (Jurassic) oceanic anoxic event. *Paleoceanography*, 23, PA4217. <https://doi.org/10.1029/2008PA001607>
- McLennan, S. M. (2001). Relationships between the trace element composition of sedimentary rocks and upper continental crust. *Geochemistry, Geophysics, Geosystems*, 2. <https://doi.org/10.1029/2000GC000109>
- McLennan, S. M., Hemming, S., McDaniel, D. K., & Hanson, G. N. (1993). Geochemical approaches to sedimentation, provenance, and tectonics. *Special Papers-Geological Society of America*, 284, 21–40. <https://doi.org/10.1130/spe284-p21>
- Meyer, K. M., Yu, M., Lehrmann, D., van de Schootbrugge, B., & Payne, J. L. (2013). Constraints on Early Triassic carbon cycle dynamics from paired organic and inorganic carbon isotope records. *Earth and Planetary Science Letters*, 361, 429–435. <https://doi.org/10.1016/j.epsl.2012.10.035>
- Montero-Serrano, J.-C., Föllmi, K. B., Adatte, T., Spangenberg, J. E., Tribouillard, N., Fantasia, A., & Suan, G. (2015). Continental weathering and redox conditions during the early Toarcian Oceanic Anoxic Event in the northwestern Tethys: Insight from the Posidonia Shale section in the Swiss Jura Mountains. *Paleogeography*,

- Palaeoclimatology, Palaeoecology*, 429, 83–99. <https://doi.org/10.1016/j.palaeo.2015.03.043>
- Newton, R. J., Reeves, E. P., Kafousia, N., Wignall, P. B., Bottrell, S. H., & Sha, J. G. (2011). Low marine sulfate concentrations and the isolation of the European epicontinental sea during the Early Jurassic. *Geology*, 39, 7–10. <https://doi.org/10.1130/g31326.1>
- Och, L. M., & Shields-Zhou, G. A. (2012). The Neoproterozoic oxygenation event: Environmental perturbations and biogeochemical cycling. *Earth-Science Reviews*, 110, 26–57. <https://doi.org/10.1016/j.earscirev.2011.09.004>
- Ossa Ossa, F. O., Hofmann, A., Wille, M., Spangenberg, J. E., Bekker, A., Poulton, S. W., ... Schoenberg, R. (2018). Aerobic iron and manganese cycling in a redox-stratified Mesoarchean epicontinental sea. *Earth and Planetary Science Letters*, 500, 28–40. <https://doi.org/10.1016/j.epsl.2018.07.044>
- Pancost, R. D., Crawford, N., Magness, S., Turner, A., Jenkyns, H. C., & Maxwell, J. R. (2004). Further evidence for the development of photic-zone euxinic conditions during Mesozoic oceanic anoxic events. *Journal of the Geological Society*, 161, 353–364. <https://doi.org/10.1144/0016764903-059>
- Pearce, C. R., Cohen, A. S., Coe, A. L., & Burton, K. W. (2008). Molybdenum isotope evidence for global ocean anoxia coupled with perturbations to the carbon cycle during the Early Jurassic. *Geology*, 36, 231–234. <https://doi.org/10.1130/g24446a.1>
- Percival, L. M. E., Cohen, A. S., Davies, M. K., Dickson, A. J., Hesselbo, S. P., Jenkyns, H. C., ... Xu, W. (2016). Osmium isotope evidence for two pulses of increased continental weathering linked to Early Jurassic volcanism and climate change. *Geology*, 44, 759–762. <https://doi.org/10.1130/g37997.1>
- Peters, K. E., Walters, C. C., & Moldowan, J. M. (2005). *The biomarker guide: Biomarkers and isotopes in petroleum systems and earth history* (2nd ed.). Cambridge, UK: Cambridge University Press.
- Pinti, D. L., Hashizume, K., Sugihara, A., Massault, M., & Philippot, P. (2009). Isotopic fractionation of nitrogen and carbon in Paleoproterozoic cherts from Pilbara craton, Western Australia: Origin of <sup>15</sup>N-depleted nitrogen. *Geochimica et Cosmochimica Acta*, 73, 3819–3848. <https://doi.org/10.1016/j.gca.2009.03.014>
- Raghoebarasingh, A. A., Pol, A., van de Pas-Schoonen, K. T., Smolders, A. J. P., Ettwig Katharina F., Rijpstra, W. I. C., ... & Strous, M. (2006). A microbial consortium couples anaerobic methane oxidation to denitrification. *Nature*, 440, (7086), 918–921. <http://dx.doi.org/10.1038/nature04617>
- Riccardi, A., Kump, L. R., Arthur, M. A., & D'Hondt, S. (2007). Carbon isotopic evidence for chemocline upward excursions during the end-Permian event. *Palaeogeography, Palaeoclimatology, Palaeoecology*, 248, 73–81. <https://doi.org/10.1016/j.palaeo.2006.11.010>
- Richo, S., van De Schootbrugge, B., Pross, J., Püttmann, W., Quan, T. M., Lindström, S., ... Hauenberger, C. A. (2012). Hydrogen sulphide poisoning of shallow seas following the end-Triassic extinction. *Nature Geoscience*, 5, 662–667. <https://doi.org/10.1038/ngeo1539>
- Röhl, H. J., Schmid-Röhl, A., Oschmann, W., Frimmel, A., & Schwark, L. (2001). The Posidonia Shale (Lower Toarcian) of SW-Germany: An oxygen-depleted ecosystem controlled by sea level and palaeoclimate. *Palaeogeography, Palaeoclimatology, Palaeoecology*, 165, 27–52. [https://doi.org/10.1016/S0031-0182\(00\)00152-8](https://doi.org/10.1016/S0031-0182(00)00152-8)
- Röhl, H. J., & Schmid-Röhl, A. (2005). Lower Toarcian (Upper Liassic) black shales of the Central European Epicontinental Basin: A sequence stratigraphic case study from the Sw German posidonia shale. *The Deposition of Organic-Carbon-Rich Sediments: Models, Mechanisms, and Consequences*, 82, 165–189. <https://doi.org/10.2110/pec.05.82.0165>
- Ruebsam, W., Mayer, B., & Schwark, L. (2019). Cryosphere carbon dynamics control Early Toarcian global warming and sea level evolution. *Global and Planetary Change*, 172, 440–453. <https://doi.org/10.1016/j.gloplacha.2018.11.003>
- Ruebsam, W., Müller, T., Kovács, J., Pálffy, J., & Schwark, L. (2018). Environmental response to the early Toarcian carbon cycle and climate perturbations in the northeastern part of the West Tethys shelf. *Gondwana Research*, 59, 144–158. <https://doi.org/10.1016/j.gr.2018.03.013>
- Ruebsam, W., Münzberger, P., & Schwark, P. (2014). Chronology of the Early Toarcian environmental crisis in the Lorraine Sub-Basin (NE Paris Basin). *Earth and Planetary Science Letters*, 404, 273–282. <https://doi.org/10.1016/j.epsl.2014.08.005>
- Ruebsam, W., Reolid, M., & Schwark, L. (2020).  $\delta^{13}\text{C}$  of terrestrial vegetation records Toarcian CO<sub>2</sub> and climate gradients. *Scientific reports*, 10, 1–8. <https://doi.org/10.1038/s41598-019-56710-6>
- Ruvalcaba Baroni, I., Pohl, A., van Helmond, N. A., Papadomanolaki, N. M., Coe, A. L., Cohen, A. S., ... Slomp, C. P. (2018). Ocean circulation in the Toarcian (Early Jurassic): A key control on deoxygenation and carbon burial on the European Shelf. *Paleoceanography and Paleoclimatology*, 33, 994–1012. <https://doi.org/10.1029/2018pa003394>
- Sahoo, S. K., Planavsky, N. J., Kendall, B., Wang, X., Shi, X., Scott, C., ... Jiang, G. (2012). Ocean oxygenation in the wake of the Marinoan glaciation. *Nature*, 489, 546–549. <https://doi.org/10.1038/nature11445>
- Sælen, G., Tyson, R. V., Telnæs, N., & Talbot, M. R. (2000). Contrasting watermass conditions during deposition of the Whitby Mudstone (Lower Jurassic) and Kimmeridge Clay (Upper Jurassic) formations, UK. *Palaeogeography, Palaeoclimatology, Palaeoecology*, 163, 163–196. [https://doi.org/10.1016/S0031-0182\(00\)00150-4](https://doi.org/10.1016/S0031-0182(00)00150-4)
- Schouten, S., van Kaam-Peters, H. M., Rijpstra, W. I. C., Schoell, M., & Damste, J. S. S. (2000). Effects of an oceanic anoxic event on the stable carbon isotopic composition of early Toarcian carbon. *American Journal of Science*, 300, 1–22. <https://doi.org/10.2475/ajs.300.1.1>
- Schwark, L., & Frimmel, A. (2004). Chemostratigraphy of the Posidonia Black Shale, SW-Germany. *Chemical Geology*, 206, 231–248. <https://doi.org/10.1016/j.chemgeo.2003.12.008>
- Shields, G., & Veizer, J. (2002). Precambrian marine carbonate isotope database: Version 1.1. *Geochemistry, Geophysics, Geosystems*, 3, 1 of 12–12 of 12. <https://doi.org/10.1029/2001GC000266>
- Song, J., Littke, R., & Weniger, P. (2017). Organic geochemistry of the Lower Toarcian Posidonia Shale in NW Europe. *Organic Geochemistry*, 106, 76–92. <https://doi.org/10.1016/j.orggeochem.2016.10.014>
- Spötl, C., & Vennemann, T. W. (2003). Continuous-flow isotope ratio mass spectrometric analysis of carbonate minerals. *Rapid Communications in Mass Spectrometry*, 17, 1004–1006. <https://doi.org/10.1002/rcm.1010>
- Suan, G., Van De Schootbrugge, B., Adatte, T., Fiebig, J., & Oschmann, W. (2015). Calibrating the magnitude of the Toarcian carbon cycle perturbation. *Paleoceanography*, 30, 495–509. <https://doi.org/10.1002/2014pa002758>
- Svensen, H., Planke, S., Chevallier, L., Malthes-Sørensen, A., Corfu, F., & Jamtveit, B. (2007). Hydrothermal venting of greenhouse gases triggering Early Jurassic global warming. *Earth and Planetary Science Letters*, 256, 554–566. <https://doi.org/10.1016/j.epsl.2007.02.013>
- Takahashi, S., Kaiho, K., Oba, M., & Kakegawa, T. (2010). A smooth negative shift of organic carbon isotope ratios at an end-Permian mass extinction horizon in central pelagic Panthalassa. *Palaeogeography, Palaeoclimatology, Palaeoecology*, 292, 532–539. <https://doi.org/10.1016/j.palaeo.2010.04.025>
- Them, T. R., Gill, B. C., Selby, D., Grocke, D. R., Friedman, R. M., & Owens, J. D. (2017). Evidence for rapid weathering response to climatic warming during the Toarcian Oceanic Anoxic Event. *Scientific Reports*, 7, 5003. <https://doi.org/10.1038/s41598-017-05307-y>
- Trecalli, A., Spangenberg, J., Adatte, T., Föllmi, K. B., & Parente, M. (2012). Carbonate platform evidence of ocean acidification at the onset of the early Toarcian oceanic anoxic event. *Earth and Planetary*

- Science Letters*, 357–358, 214–225. <https://doi.org/10.1016/j.epsl.2012.09.043>
- Tribouillard, N., Algeo, T. J., Lyons, T., & Riboulleau, A. (2006). Trace metals as paleoredox and paleoproductivity proxies: An update. *Chemical Geology*, 232, 12–32. <https://doi.org/10.1016/j.chemgeo.2006.02.012>
- Ullmann, C. V., Thibault, N., Ruhl, M., Hesselbo, S. P., & Korte, C. (2014). Effect of a Jurassic oceanic anoxic event on belemnite ecology and evolution. *Proceedings of the National Academy of Sciences of the United States of America*, 111, 10073–10076. <https://doi.org/10.1073/pnas.1320156111>
- Ulrich, T., Kamber, B. S., Woodhead, J. D., & Spencer, L. A. (2010). Long-term observations of isotope ratio accuracy and reproducibility using Quadrupole ICP-MS. *Geostandards and Geoanalytical Research*, 34, 161–174. <https://doi.org/10.1111/j.1751-908X.2010.00046.x>
- van Breugel, Y., Baas, M., Schouten, S., Mattioli, E., & Sinninghe Damsté, J. S. (2006). Isorenieratane record in black shales from the Paris Basin, France: Constraints on recycling of respired CO<sub>2</sub> as a mechanism for negative carbon isotope shifts during the Toarcian oceanic anoxic event. *Paleoceanography*, 21, PA4220. <https://doi.org/10.1029/2006pa001305>
- van de Schootbrugge, B., & Gollner, S. (2013). Altered primary production during mass-extinction events. *The Paleontological Society Papers*, 19, 87–114. <https://doi.org/10.1017/S1089332600002709>
- van de Schootbrugge, B., McArthur, J. M., Bailey, T. R., Rosenthal, Y., Wright, J. D., & Miller, K. G. (2005). Toarcian oceanic anoxic event: An assessment of global causes using belemnite C isotope records. *Paleoceanography*, 20, PA3008. <https://doi.org/10.1029/2004pa001102>
- Watanabe, Y., Naraoka, H., Wronkiewicz, D. J., Condie, K. C., & Ohmoto, H. (1997). Carbon, nitrogen, and sulfur geochemistry of Archean and Proterozoic shales from the Kaapvaal Craton, South Africa. *Geochimica et Cosmochimica Acta*, 61, 3441–3459. [https://doi.org/10.1016/S0016-7037\(97\)00164-6](https://doi.org/10.1016/S0016-7037(97)00164-6)
- Wignall, P. B., Hallam, A., Newton, R. J., Sha, J. G., Reeves, E., Mattioli, E., & Crowley, S. (2006). An eastern Tethyan (Tibetan) record of the Early Jurassic (Toarcian) mass extinction event. *Geobiology*, 4, 179–190. <https://doi.org/10.1111/j.1472-4669.2006.00081.x>
- Xu, W., Ruhl, M., Jenkyns, H. C., Hesselbo, S. P., Riding, J. B., Selby, D., ... Idiz, E. F. (2017). Carbon sequestration in an expanded lake system during the Toarcian oceanic anoxic event. *Nature Geoscience*, 10, 129–134. <https://doi.org/10.1038/ngeo2871>
- Xu, W., Ruhl, M., Jenkyns, H. C., Leng, M. J., Huggett, J. M., Minisini, D., ... Hesselbo, S. P. (2018). Evolution of the Toarcian (Early Jurassic) carbon-cycle and global climatic controls on local sedimentary processes (Cardigan Bay Basin, UK). *Earth and Planetary Science Letters*, 484, 396–411. <https://doi.org/10.1016/j.epsl.2017.12.037>
- Ziegler, P. A. (1988). Evolution of the Arctic-North Atlantic and the Western Tethys. *AAPG Memoir*, 43, 198.

### SUPPORTING INFORMATION

Additional supporting information may be found online in the Supporting Information section.

**How to cite this article:** Wang Y, Ossa Ossa F, Wille M, et al. Evidence for local carbon-cycle perturbations superimposed on the Toarcian carbon isotope excursion. *Geobiology*. 2020;18:682–709. <https://doi.org/10.1111/gbi.12410>